THESIS

AN ULTRA-HIGH RESOLUTION PULSED-WIRE MAGNET MEASUREMENT SYSTEM

Submitted by

Alex D'Audney

Department of Electrical and Computer Engineering

In partial fulfillment of the requirements

For the Degree of Master of Science

Colorado State University

Fort Collins, Colorado

Spring 2016

Master's Committee:

Advisor: Stephen Milton
Co-Advisor: Sandra Biedron

Tom Johnson

ABSTRACT

AN ULTRA-HIGH RESOLUTION PULSED-WIRE MAGNET MEASUREMENT SYSTEM

The performance of a Free-Electron Laser (FEL) depends in part on the quality of the magnetic field in the undulator. Ideally the magnetic field on the axis of the undulator is transverse to the axis and sinusoidally varying due to the periodic sequence of alternating field dipole magnets. The resulting ideal trajectory of a relativistic electron bunch traveling along the axis is also sinusoidal in the plane perpendicular to that of the ideal magnetic field. Imperfections in the magnetic field lead to an imperfect electron trajectory, both offset and angle, as well as a relative phase error between the oscillation phase of the electrons and the generated electromagnetic field. The result of such errors is a reduction of laser gain impacting overall FEL performance.

A pulsed-wire method can be used to determine the profile of the magnetic field. This is achieved by sending a square-current pulse through a wire placed along the length of the axis that will induce an Lorentz-force interaction with the magnetic field. Measurement of the resulting displacement in the wire over time using a motion detector yields the first or second integrals of the magnetic field and so provides a measure of the local magnetic field strength. Dispersion in the wire can be corrected using algorithms, with a resulting increase in overall accuracy of the measurement. Once the fields are known, magnetic shims can be placed to correct the magnetic fields to the desired level. In this thesis we will describe the design, construction and testing of a pulsed-wire magnetic measurement system and use this system to characterize the CSU FEL undulator.

TABLE OF CONTENTS

INTRODUCTION

Synchrotron Radiation

History

Synchrotrons were first built in the late 1940s for the purpose of high-energy physics experiments. In any synchrotron there is a natural byproduct called synchrotron radiation (SR). This comes about due to the strong transverse acceleration of the electrons traversing the magnetic dipole fields, and it was unwanted by high-energy physicists as it limited the maximum energy achievable from an electron synchrotron. It was discovered later that this radiated energy could be useful for other experiments and applications. Synchrotron radiation experiments became so popular that facilities were built solely for that purpose. Insertion devices known as undulators can be used within a storage ring to enhance the light characteristics for the synchrotron radiation light users. They create much more monochromatic and brilliant light than bending magnets alone [1]. An in-depth description of undulator characteristics and emitted light will be discussed in later sections.

Synchrotron Light Sources

The performance of an electron, accelerator-based, light-source facility, either a synchrotron radiation light source or free-electron laser (FEL), to be more thoroughly described later), depends in part on the quality of the magnetic field in an undulator magnet. An example schematic layout of a synchrotron light source that exploits the use of undulator devices is shown in Figure 1. The accelerator systems in a facility like this increases the total energy, E, of the electrons to the desired value and maintains the energy at this level. These electrons are passed through the fields of the various undulators and the resulting light is then guided to the

user experiments. Such light sources are used for several research activities including medicine, security and defense, discovery science, and industry [3]. These users desire high photon brilliance, defined as the number of photons/second/mm^2/mrad^2/(0.1% bandwidth), for their experiments, and this is achieved by both ensuring a high quality of electron performance as well as high-quality undulator fields.

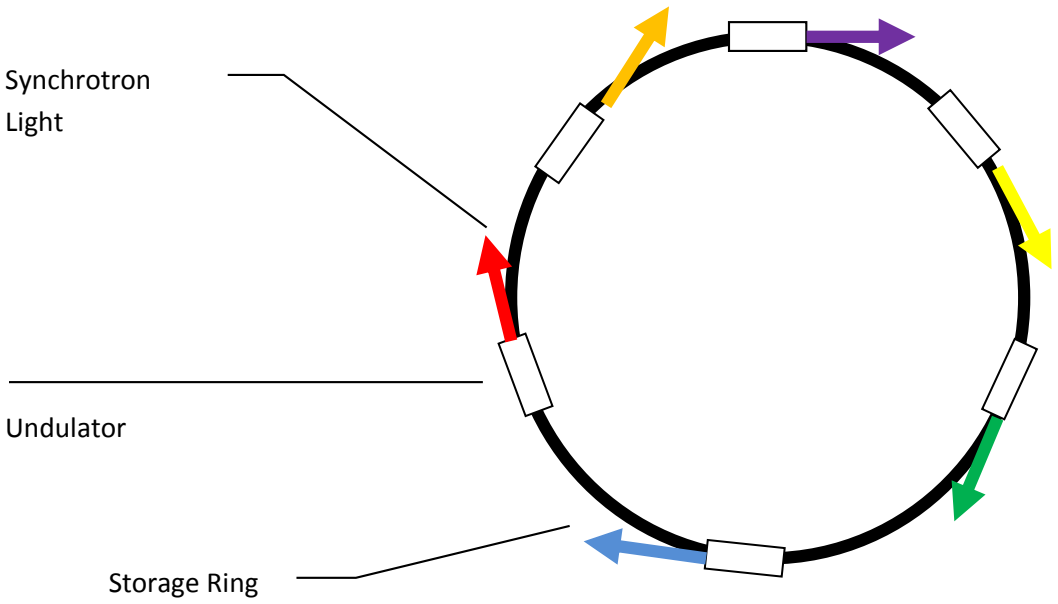

Figure 1: An overview of a modern synchrotron light source facility. Many beamlines, shown as colored areas and each autonomous to one another, are provided to the large user community [2].

Free-Electron Lasers

An FEL is another type of synchrotron light source that utilizes coherence effects to greatly amplify the light beyond that of more conventional incoherent synchrotron radiation-based light sources. This amplification is the result of forcing all electrons within a single bunch to emit coherently (i.e. in phase). This process comes about by allowing the electrons to

interact with the emitted radiation in a manner that forces some electrons to gain energy while others to lose energy. This difference manifests itself in a microbunching of the electrons within the bunch at a period equal to the resonant wavelength. Once this occurs the electrons within each microbunch emit coherently and a very large enhancement of the radiation is achieved. [4,5]. Once again both high-quality electron beams and high-quality undulator magnets are needed to ensure that the FEL process functions at a high level of performance.

Radiation Characteristics: Basics

Dipoles

The emitted radiation of an electron from a bending magnet has a broad spectral bandwidth with a characteristic photon energy of $\epsilon_c = 0.665 B_0 E^2 [\mathrm{keV}]$, where B_0 is the magnetic field strength in Tesla and E is the electron's energy in GeV [1]. Using nominal numbers of 3 GeV and 1 T one readily finds that the characteristic photon energy is roughly 6 keV, i.e. hard x-rays. As an interesting side comment, consider a storage ring. One can make a rough estimate of the energy loss per turn for a single electron propagating around a storage ring. The appropriate formula is $U_0 = \frac{C_\gamma E^4 [\mathrm{GeV}]}{\rho_0 \, [\mathrm{m}]}$ where $C_\gamma = 8.85 \times 10^{-5} \, [\frac{\mathrm{m}}{\mathrm{GeV}^3}]$ [7]. In this example case the radius of curvature ρ_0 is roughly equal to 10 m and the energy lost by a single electron per revolution is 700 keV. This energy must be replaced every turn or the electron will rapidly loose energy and be lost to the machine aperture. One should also note the strong quartic dependence on the electron beam energy. This is the primary limitation for the operation of electron storage rings at energies above a few hundred GeV. The losses become tremendous and it becomes physically impossible on a terrestrial scale to make a machine with a large enough radius to compensate adequately the power loss.

Undulators

The desire to use undulator magnets in light sources can be understood by considering the radiation emitted by such devices compared to that of an ordinary dipole. Relativistic effects cause the emitted radiation to be strongly focused in the forward direction. The electromagnetic radiation from a relativistic electron undergoing strong transverse acceleration that occurs in an N-period undulator has a basic opening angle of $\frac{2}{\gamma\sqrt{N}}$ and is much less than the opening angle of a dipole ($\frac{1}{\gamma}$), where γ is the is the normalized energy of the electron [8]. The differences between undulator and dipole radiation characteristics is shown in Figure 2.

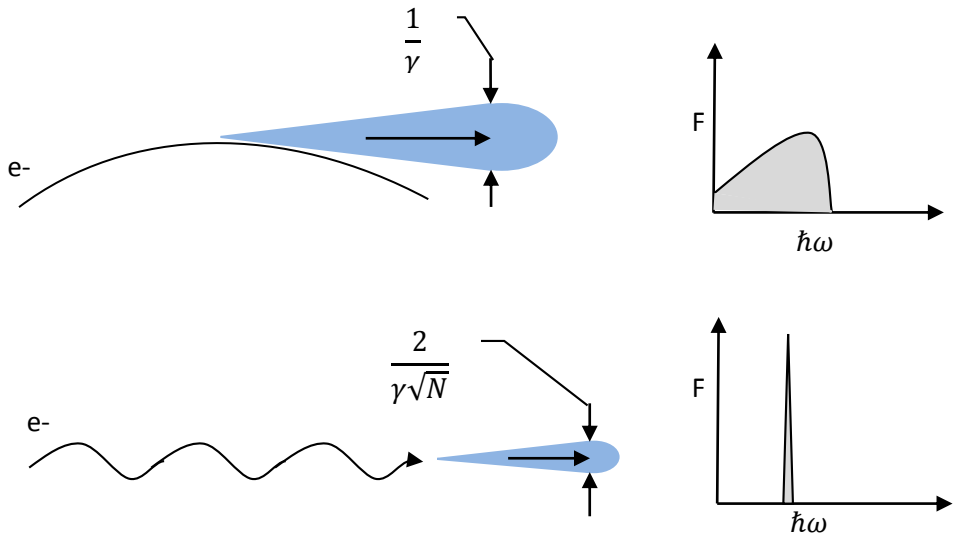

Figure 2: EM radiation patterns and spectra from a dipole bending magnet (top) and undulator magnet (bottom) [8].

To understand the spectral benefits of undulator radiation, first consider a single dipole magnet, where a single very short pulse is generated. If one directs this single short pulse

through a spectrometer and views the result one sees a broad continuum with a characteristic wavelength. Now consider an undulator magnet. If one places a number of magnets in a row that alternate in sign then one gets a series of short pulses of alternating electric field sign. Once again if one directs these light pulses into a spectrometer then the once broad continuum of the dipole magnet radiation now has a periodic component to it that manifests itself as a resonant peak at a wavelength corresponding to parameters of both the undulator magnet and the electron beam energy. The net result is a significant increase in photon brightness at this resonant wavelength as well as harmonics of this resonant wavelength as can be seen on the right side of Figure 2. Utilizing such features of the radiation, undulator magnet-based systems can achieve a much higher brightness and flux than bending magnets alone.

Undulators

Physical Characteristics and Properties

Undulator magnets are designed with dipole fields of alternating signs, with the net result producing an on-axis sinusoidally varying field along the length of the undulator (Figure 3).

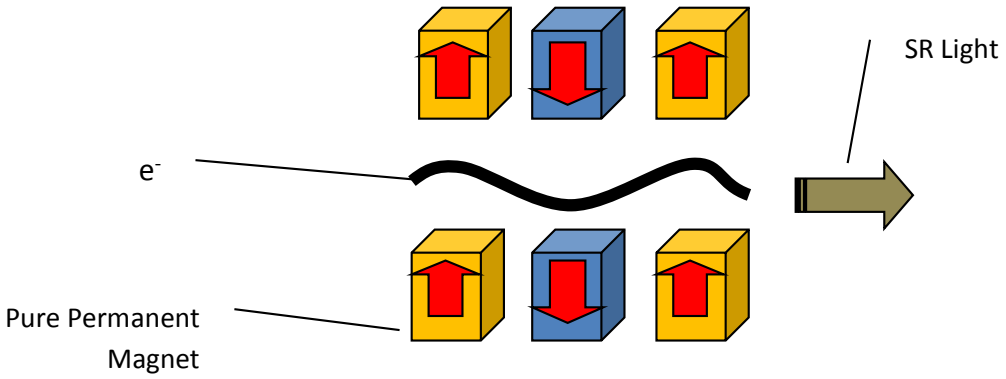

Figure 3: The basic undulator magnet [9].

Electrons passing along this axis are then transversely accelerated and emit synchrotron radiation. The emitted light due to the electron passing through the field of an undulator can be described by looking at the relativistic electrons' interaction with the magnetic field. The moving electrons witness the undulator in their own frame of reference. The relativistic (Lorentz) frame change rules will cause the electrons to witness an oscillating electric field in the perpendicular direction, as well as the magnetic field. The electrons will emit light at the same wavelength as the electromagnetic wave in the electron's frame. The wavelength in the laboratory frame is altered due to the Doppler Effect and its resulting optical wavelength is:

$$\lambda_{rn} = \frac{\lambda_u}{2n\gamma^2}\left(1 + \frac{K^2}{2}\right) \quad (1)$$

where λ_{rn} is the so-called resonant wavelength at harmonic n, λ_u is the period of the undulator field, $\gamma = \frac{E}{mc^2}$ is the relativistic normalized energy of the electron, and K is the normalized magnetic field strength of the undulator [11, 12].

As can been seen from Equation 1, the wavelength of the radiated light depends on the wavelength and field strength of the undulator, as well as the electron energy. Varying these parameters will change the wavelength of light that is being emitted.

There are many types of undulators available depending on the specifications and capabilities of the user. The two main types of undulators are constructed using permanent magnets or electro-magnets. The undulators energized using permanent magnets can be further separated into two primary varieties: pure permanent magnet (PPM) and hybrid undulators. In the case of the PPM one uses nothing but permanent magnets to shape the field, while in the case of the

hybrid one uses high permeability materials such as vanadium permendur along with the permanent magnets to shape the fields. In addition super-conducting, electro-magnet, undulators have been used to achieve very high fields while at the same time maintaining a reasonable aperture for the electron beam to pass through. Undulators can also be built using various field orientations depending on the desire of the end user of the radiation.

Undulator Errors

Trajectory Error

An ideal undulator would provide the perfect field for light generation; however, there are always errors in the field. The impact of these errors and how one measures and corrects them must be understood. We are concerned with both trajectory errors and phase errors within the undulator. Trajectory errors are simple to understand. If one of the dipole fields within the undulator has an incorrect strength, then the electron gets an incorrect total kick (angle change) upon passage of that dipole. Now pointed in a slightly wrong direction the electron's average trajectory starts to deviate from the ideal undulator axis and the generated light starts to point in a direction different from before therefore reducing the opportunity for overlap between the EM wave and the electron bunch.

Phase Error

Phase errors are a little more difficult to understand. Imagine the electron following an ideal sinusoidal trajectory with fixed amplitude of oscillation. The ultrarelativistic electron is moving at essentially the speed of light; however, its average forward velocity is slower due to the path length along the sinusoid. The resonant wavelength condition comes about from the condition that the light out paces the electron by one optical period for every undulator period

of travel. If, however, there is a period in the undulator that has low field, then the electron will have a higher average longitudinal velocity and the phase condition will not be correct for the resonant condition. This is a phase error.

The result of phase errors is important in both incoherent and coherent (such as an FEL) sources. In incoherent sources such as the APS facility there is the desire by many users to capitalize on the higher harmonics of the radiation. A 20-degree rms phase error at the fundamental wavelength is a 180 degree phase error at the 9th harmonic and thus washes out emission at the harmonic entirely. In an FEL the phase errors reduce the effective coupling between the electrons and the EM wave causing a reduction in the energy transfer from the e-beam to the optical field and hence, reduces FEL gain [4,5,7-12]. In fact, a bad phase error can result in energy being removed by the electrons from the EM wave resulting in negative gain. Thus, minimizing the phase errors in an undulator is extremely important.

Undulator Characterization

To minimize errors within the undulator, the magnetic field must first be characterized. Traditionally, the fields within these devices have been measured with high accuracy using a Gauss meter or Hall probe [13-14]; however, with more complex undulator designs being used today, these types of probe systems may not always be a viable option. Undulator topologies such as narrow undulator gaps, cryogenic environments in superconducting undulators, or other confining configurations restrict measurement access. A pulsed-wire method is an attractive option to map the magnetic field in a noninvasive manner [15-17].

A Hall probe and Gauss meter are typically used to measure the field of an undulator. The probe, mounted on a translation stage, is moved along the undulator axis measuring the

field as a function of the longitudinal position. Figure 4 shows an example of this process. The picture was taken by the author's advisor (Stephen Milton) in Shanghai, China. With this information the field and phase errors can be determined. This method has been a proven technique to accurately characterize the field in an undulator magnet [14]. However, it does not lend itself well to certain mechanical configurations, whereas a pulsed-wire method can be very effective.

Figure 4: Hall probe measurement process of an undulator magnet.

In the pulsed-wire method, a current pulse is passed through a tensioned wire that is located along the axis of the undulator. Due to the Lorentz force [12],

$$\vec{F} = q\vec{E} + q\vec{v} \times \vec{B} \quad (2)$$

the amount of local force generated on the wire is proportional to the magnitude of the local transverse magnetic field component, $\vec{B}$, as well as the current in the wire, $I \propto qv$. The wire will not stay displaced after the pulse, and an acoustic wave will travel along the wire and out of the undulator in both directions. This signal is directly related in time to the strength and position of the magnetic field. Depending on the length of the pulse introduced in the wire, either the first or second integral of the magnetic field can be deduced. These integrals correspond to both the trajectory angle and the position of an electron as it propagates through the undulator and can be used to identify both field and phase errors in the magnetic field profile. The first and second field integrals can be determined directly by introducing short (microseconds) and long (milliseconds) pulses respectively. The length of the long current pulse as well as the length of the wire in the setup is based on the length of the undulator. The wire must be long enough so that reflections from the end points of the setup do not interfere with the signal being measured. For the long pulse to be effective, the pulse must be "on" long enough for the acoustic signal to pass the detector. The length of the short pulse is determined by both the speed of the acoustic wave and the frequencies we wish to measure. The pulse should be short compared to the time it takes for the acoustic wave to move a small fraction of one period of the undulator; however, one does not want to make this pulse too short as the total impulse imparted to the wire is proportional to the current integral. More details will be provided in the coming chapters.

THE CSU UNDULATOR

The undulator being tested here, shown in Figure 5 (left), was previously used in a functional FEL system at the University of Twente, Netherlands [19]. The topography is such that the use of a Hall probe to measure the field is impossible. From Figure 5 (right), one can see the large blocks holding the undulator's gap steady. These prevent a Hall probe from being readily inserted along the magnetic axis. Here a pulsed-wire method is clearly useful for the characterization of the field. Previously, scientists at the University of Twente used the pulsed-wire method to characterize and correct the fields [15]. However, these measurements did not compensate for dispersion, so a more accurate measurement is needed before the undulator can be operated with peak performance. Also, the entire FEL system was shipped in a container from the Netherlands to the CSU campus. The rigorous journey dislodged some previously aligned magnetic shims, requiring the need for new measurements. A well-documented and reproducible characterization method is important for future measurements as well as possible student experiments.

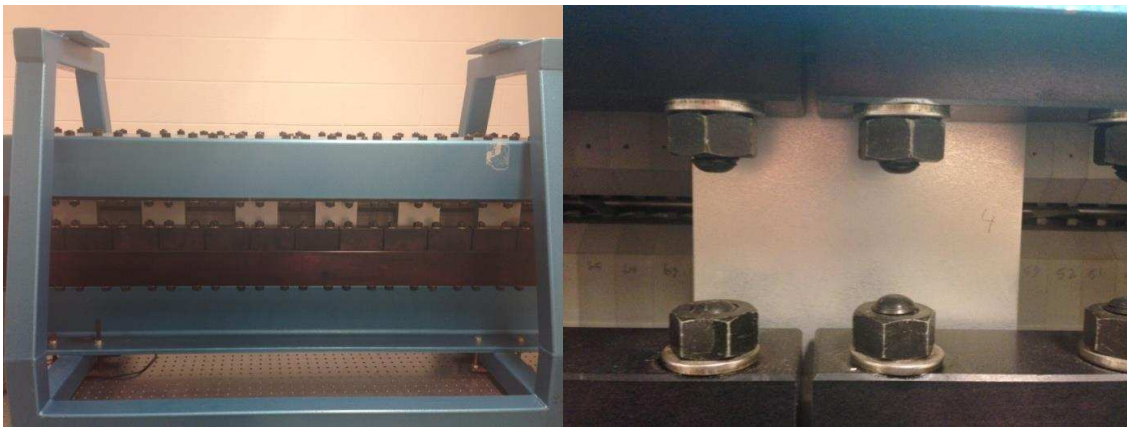

Figure 5: Left, CSU's undulator. Right, zoom to see gap gauge blocks.

Description of Thesis

This thesis describes a pulsed-wire magnet measurement system that was developed between summer 2013 and spring 2015. The undulator under test is described in a later chapter. This pulsed-wire method which we will use overcomes two effects, dispersion in the wire and finite pulse width, which have previously limited this method's accuracy in characterizing the magnetic field in an undulator [20]. The principal concept behind this technique is to use a thin current-carrying wire to simulate both the transverse velocity and oscillation trajectory of a charged particle passing along the axis of the undulator. We will first describe the pulse-wire method giving a bit of history and explaining the essential equations used to accurately determine the field from the measurements. We will next give a brief description of the undulator we measured, and this will be followed by a detailed description of the experimental process and the results of the measurement. And finally we will draw some conclusions and provide some recommendations for going forward.

Simple History

The pulsed-wire concept was first developed by R. W. Warren at Los Alamos National Laboratory [21]. It has since been used in a variety of specialized cases in the characterization of a variety of magnetic fields including undulators. Limitations on the method's accuracy due to dispersive effects in the wire and the finite pulse width can now be corrected using mathematical algorithms applied to the data [20]. A simplified setup of a pulsed-wire system is shown in Figure 6 [22]. All components and procedures of this system will be explained in detail in later sections.

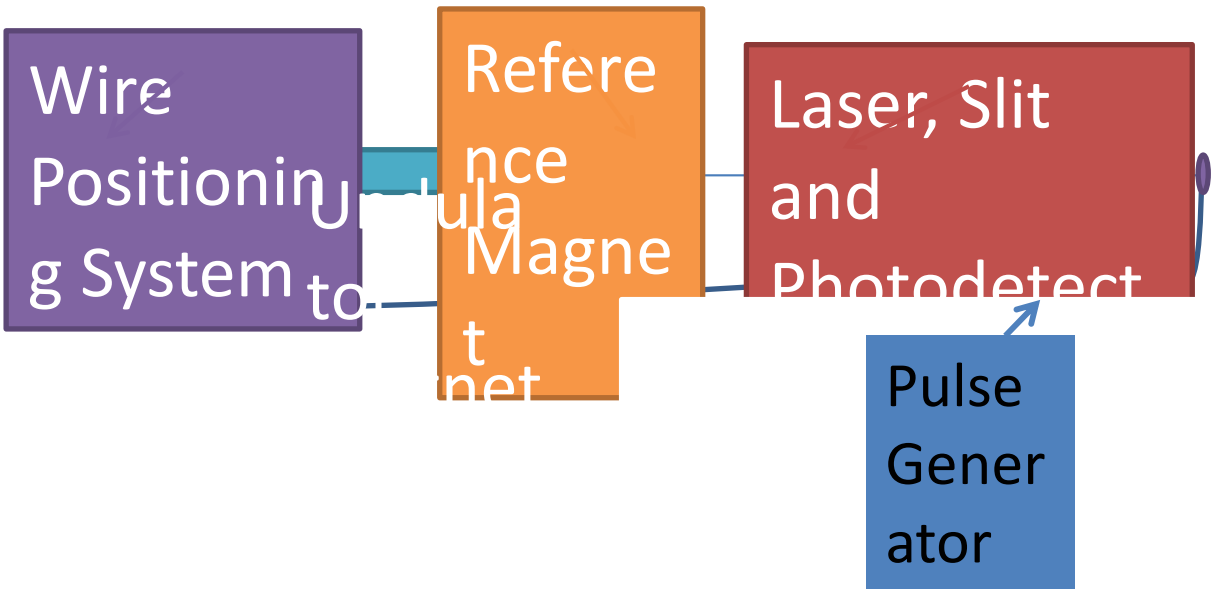

Figure 6: Simplified pulsed wire setup.

Basic Understanding

The vibration of a current-carrying, tensioned, wire due to the Lorentz force is the basis of the puled-wire method. The amplitude of these vibrations, or wire displacement, depends on the strength of the magnetic field being applied and the amount of current in the wire. Using appropriate current pulses both the first and second field integrals can be deduced from measurement of the wire's displacement [23,24]. To get an absolute calibration a known reference magnetic field is first characterized using both the pulsed-wire method and a Hall probe.

Some specifications must be followed to properly deduce the field integrals. First, the setup must be built such that reflections of the acoustic wave from the end wire mounts are not measured. Since the disturbance travels in both directions at the same velocity, the wire must be twice as long as the undulator. With a total undulator length of 1.25m, the pulsed wire setup must be at least 2.50m. However, due to the addition of the reference magnet we did not place the undulator directly at one end point of the setup. This increased the total length of the setup to 3m. Second, the proper width of the pulses must be set to accurately determine the first and second field integrals.

To measure the 1st field integral one must use a short pulse. The short pulse must satisfy the relation $\omega_{max}\delta t < 2\pi$ [20]. To find δt, we must determine how long it takes for the pulse to traverse one period of the undulator. The wave speed is directly related to the tension of the wire in the system. As an example, we will select the wave speed to be $v = 100\frac{m}{s}$ which is close to the experimental value found later. Since we want a resolution better than 1/10 of a period, we can then determine what the pulse width should be. The undulator has a period of

2.5 cm, so we want a resolution greater than 0.25 cm. So, $\delta t < \frac{period}{v} = \frac{0.25cm}{100\frac{m}{s}} = 25\mu s$. A pulse length of $20\mu s$ was chosen to fulfill this relation.

A long pulse must be used to measure the 2nd field integral. The determination of long is in terms of the length of the undulator and how long it takes for the acoustic wave to travel the length of the undulator. The long pulse must follow:

$$c_0 \delta t > N\lambda_u = 50 * 25mm = 1.25m$$

Where $c_0 = 170\,\frac{m}{s}$. So the pulse length must be:

$$\delta t > \frac{1.25}{170} s > \mathbf{7.35ms}$$

A value of 12 ms was chosen and sufficient for the length of the long pulse for the experiments.

Output

Field Integrals

As said earlier, the first and second magnetic field integrals of the undulator provide the corresponding velocity and position of the electron respectively. To see this, assume that the magnetic field on axis in the undulator is in the vertical direction only (we will call this the y axis), $B = B_y(z)$ as seen in Figure 7. Next assume that the electron enters the undulator field on the undulator magnetic axis and travels along the z coordinate and that it has a fixed total momentum. The static magnetic field cannot change the electron's total momentum, but it can, through the Lorentz force, change the direction of the momentum.

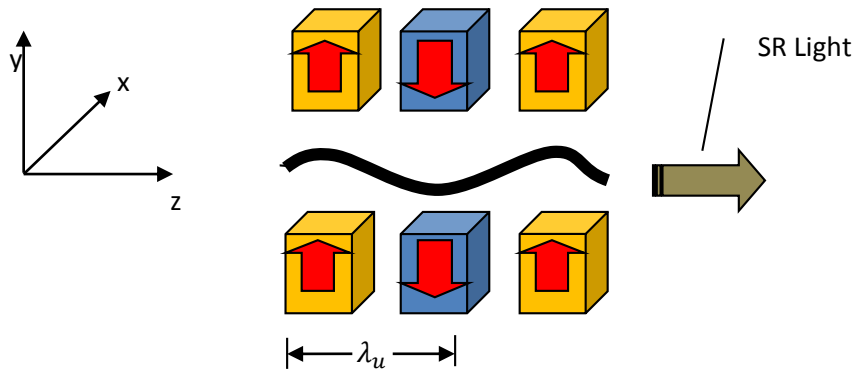

Figure 7: Characteristics of the beam in an undulator [11].

By looking at the forces acting on the electron the velocity and position can be determined. As stated earlier, the only force acting on the electron is the Lorentz Force. Thus, the work can be written as:

$$\vec{F} \cdot \vec{v} = [B_y \times (v_x + v_z)] \cdot (v_x + v_z) = 0. \tag{3}$$

This shows that there is no work done on the electron due to the magnetic field. No work corresponds to zero energy being added to the electron, so the energy of the electron remains constant, implying that |v| is constant and therefore gamma is constant.

We need to deduce the velocity in the x-direction, $v_x(z)$. We start with the basic equation of motion for an electron

$$\vec{F} = \frac{d\vec{p}}{dt} = \frac{d(m_e \gamma \vec{v})}{dt}. \tag{4}$$

Simplifying, the right side of the equation becomes

$$\frac{d(m_e \gamma \vec{v})}{dt} \rightarrow m_e \frac{d\gamma \vec{v}}{dt} \rightarrow m_e \gamma \frac{d\vec{v}}{dt}. \tag{5}$$

Since the only force acting on the electron is the Lorentz Force the equation of motion becomes

$$\gamma m_e \frac{d\vec{v}}{dt} = q\left(\vec{B} \times \vec{v}\right)$$

Where $\vec{v} = v_x\hat{x} + v_z\hat{z}$. Performing the cross product, the equation becomes

$$\gamma m_e \frac{d(v_x\hat{x}+v_z\hat{z})}{dt} = q(B_y v_z\hat{x} - B_y v_x\hat{z}). \quad (6)$$

The two resulting equations are coupled, but some additional approximations can be made based on the fact that the electron velocity in the z-direction is much larger than the resulting wiggle motion in the x-direction. As we are interested in the motion in the x-direction we can look at that part of the equation first.

$$\gamma m_e \frac{dv_x}{dt} = qB_y(z)v_z. \quad (7)$$

The v_x derivative can be rewritten as $\frac{dv_x}{dt} = \frac{dv_x}{dz}\frac{dz}{dt}$, such that

$$\gamma m_e \frac{dv_x}{dz}\frac{dz}{dt} = qB_y(z)v_z. \quad (8)$$

Since

$$\frac{dz}{dt} = v_z, \qquad \gamma m_e \frac{dv_x}{dz} = qB_y(z). \quad (9)$$

If equation 9 is integrated one time with respect to z and solved for v_x,

$$v_x(z) = v_x(0) + \frac{1}{\gamma m_e}\int_0^z qB_y(\tilde{z})d\tilde{z}\,. \quad (10)$$

Thus, the x-velocity profile of the electron is based on the first integral of the magnetic field, plus a constant. The constant $v_x(0)$ can be set to zero if the electron beam is injected on the z-axis.

Now that one has the electron's horizontal velocity within the undulator one can determine its position by analyzing Equation 10 further, assuming $v_x(0) = 0$, such that:

$$v_x(z) = \frac{dx}{dt} = \frac{1}{\gamma m_e}\int_0^z qB_y(\tilde{z})d\tilde{z}. \tag{11}$$

The derivative can be rewritten as $\frac{dx}{dt} = \frac{dx}{dz}\frac{dz}{dt}$ so that (11) becomes:

$$\frac{dx}{dv}v_z = \frac{1}{\gamma m_e}\int_0^z qB_y(\tilde{z})d\tilde{z}. \tag{12}$$

This can now again be integrated as a function of z to become:

$$x(z) = \frac{1}{\gamma m_e v_z}\iint_0^z qB_y(\tilde{z})d\tilde{z}d\hat{z}. \tag{13}$$

This equation shows that within these assumptions the position of the electron within the undulator correlates to the second integral of the magnetic field.

Now that the field integrals have been determined from relativistic electron theory, they need to be correlated to the movement of the wire in the pulsed-wire method. As stated previously, the first or second integral can be found by introducing a short or long pulse in the wire. From Warren, it was shown that the short pulse results in a displacement of the wire, $u_{s0}(t)$, that follows

$$u_{s0}(t) = \frac{Ic_0\delta t}{2T}\int_0^{c_0 t} B(\tilde{x})d\tilde{x}\ , \tag{14}$$

where I [A] is the current in the wire in, c_0 [m/s] is the wave speed in the wire, δt [s] is the current pulse width, and T is the tension in the wire. Similarly a long pulse introduced in the wire gives a displacement of

$$u_{s0}(t) = \frac{I}{2T}\int_0^{c_0 t}\int_0^{\hat{x}} B(\hat{x})d\hat{x}d\tilde{x}. \quad (15)$$

Equations 14 and 15 are the experimental equivalents to equations 11 and 13 respectively. This shows that the 1st and 2nd field integrals can be determined from the pulsed wire method using different pulse lengths.

Limitations

Unfortunately, finite pulse width and dispersive effects have limited the accuracy of this method's results. This phenomenon causes the acoustic wave speed within the wire to be dependent on frequency. The effect on the measured signal is shown in Figure 8. Here the signal should look like a single unipolar pulse, but as is seen, with the velocity frequency dependent the pulse loses its unipolar-like signal and the signal shape changes as a function of the time dependence on the distance between the signal source and the detector.

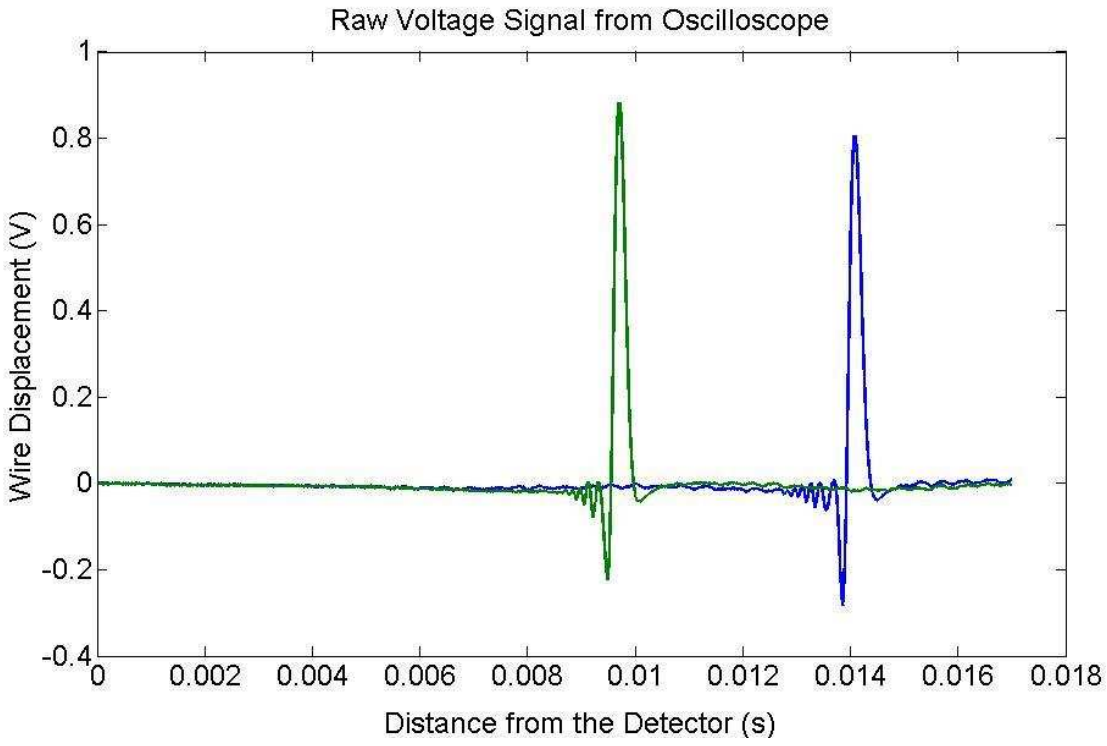

Figure 8: Dispersion effects in the wire. As the detector get further away from the source, the effects become larger.

Dispersion Correction

Precisely correlating the electron beam motion to that of the wire is a crucial aspect of the pulsed-wire concept. To do this the dispersion must be compensated for. Recently, an efficient algorithm was developed by D. Arbelaez et al. at Lawrence Berkley National Laboratory [20]. The dispersion corrected results were shown to match very closely the field profiles of those measured with a Hall probe, proving the method's effectiveness.

Dispersion Correction Equations

The algorithm derived by D. Arbelaez et al. is described in more detail in appendix A. The key features needed for the Matlab code are given in this section. Here we only give a summary of the essential components of the correction algorithm.

First the wave speed needs to be determined. This can be, and will be, done experimentally, but theoretically, using the Euler-Bernoulli theory for the bending of thin rods, a value of the wave speed as a function of wavenumber is found to be

$$c(\kappa) = c_0\sqrt{1 + \frac{EI_w}{T}\kappa^2}. \tag{16}$$

Where $c_0 = \sqrt{T/\mu}$, T is the wire tension, μ is the density of the wire, *E* is the wire's Young's modulus, EI_w is the flexural rigidity of the wire, and κ is the wave number. This is what we expect to find; however, we do not have absolute measurements of μ or EI_w. An experimental determination of *c* is therefore needed.

The experimental value for the wave speed, *c*, uses two pulsed-wire measurements displaced some Δz away from each other. These signals are transferred into the frequency domain by use of an FFT. The conjugate of the first measurement is then multiplied by the displaced measurement and yields

$$\bar{u}_s^*(\omega)\bar{u}_{s\Delta z}(\omega) = |G(\omega)|^2 e^{i\kappa\Delta z}. \tag{17}$$

This says that the product has an amplitude, $|G(\omega)|^2$, and phase, $\phi = \kappa\Delta z$. By using the relation that $\omega = c\kappa$, the wave speed can be found:

$$c = \frac{\omega \Delta z}{\phi} \tag{18}$$

This experimental wave speed determination can be compared to the theoretical values. In fitting the data to the form of equation 18 one can find both EI_w and C_o.

The short pulse case will be analyzed first. For calculational purposes a more useful description of the displacement of the wire due to the short pulse is

$$u_s^{short}(t) = \frac{I\delta t}{2\mu} \int_{-\infty}^{+\infty} \frac{i}{\kappa c_0^2} \bar{B}(\kappa) e^{-i\omega t} d\omega. \tag{19}$$

Here we will define

$$H^{short}(\kappa) = \frac{I\delta t}{2\mu} \frac{i}{\kappa c_0^2} \bar{B}(\kappa). \tag{20}$$

The scaling factor needed to obtain a dispersion corrected solution for the short pulse is

$$F^{short}(\kappa) = \frac{H_0(\kappa)}{H(\kappa)} = \left(\frac{c(\kappa)}{c_0}\right)\left(\frac{c(\kappa)+\kappa\frac{dc}{d\kappa}}{c_0}\right)\frac{i\omega(\kappa)\delta t}{e^{i\omega(\kappa)\delta t}-1}. \tag{21}$$

The non-dispersive wire displacement becomes

$$u_{s0}(t) = \int_{-\infty}^{+\infty} F(\kappa)H(\kappa)e^{-i\omega t} d\omega = \int_{-\infty}^{+\infty} H_0(\kappa)\, e^{-i\omega t} d\omega. \tag{22}$$

This equation is used for both the short and long pulse, with different scaling factors for each. For the long current pulse, the scaling factor is defined as

$$F^{long}(\kappa) = \frac{H_0(\kappa)}{H(\kappa)} = \left(\frac{c(\kappa)}{c_0}\right)^2 \frac{c(\kappa)+\kappa\frac{dc}{d\kappa}}{c_0}. \tag{23}$$

The local magnetic field profile can then be found from the dispersion corrected displacement due to a short pulse gained from equation 22. The $u_{s0}(t)$ term is utilized in equation 14 to find the magnetic field as a function of distance.

THE CSU FEL AND UNDULATOR

Our system at Colorado State University (CSU) utilizes a linear accelerator (linac) to raise the electron beam energy up to its desired level. Linacs utilize a single pass of the electron bunch along a straight line instead of many passes around a ring such as the APS accelerator system. In a linac system, the undulator is placed at the end of the beamline to create to generate the light.

The linac system at CSU is a part of the Advanced Beam Laboratory (ABL) which incorporates both accelerator and laser technologies. By utilizing both in a single facility, the two technologies can be used in a synergistic manner to perform unique experiments. The ABL will train all levels of students as well as engineers and physicists in beam science and accelerator engineering. The goal of the ABL is to realize current trends and desires in accelerator technology. These include creating a small, efficient and cost effective accelerator. The CSU linac has specifications as described in Table 1 [19].

Table 1: CSU Linac Characteristics	
Energy	6 MeV
Number of Cells	5 ½
RF Frequency	1.3 GHz

The CSU undulator's specifications are described in this chapter, including the design features from the University of Twente. This undulator is a hybrid-type permanent magnet device containing 50 periods. Each period has a length of λ_u =25mm. A hybrid undulator is made

up of alternating high permeability poles and permanent magnets. The magnetic material is Sm_1Co_5 and the poles are vanadium permendur. This results in a peak on-axis magnetic field of 0.61T at an 8mm gap. The optimized design parameters are listed in Table 2 [15]. The undulator poles were shaped to utilize parabolic pole focusing. The circular pole shape adds a sextupole contribution to the conventional undulator field and creates equal focusing in both transverse directions. This transverse focusing is essential for our low energy beams in order to ensure proper guiding of the beam along the length of the undulator and prevent beam losses within the undulator [25, 26]. The curvature of the pole can be seen in Figure 9.

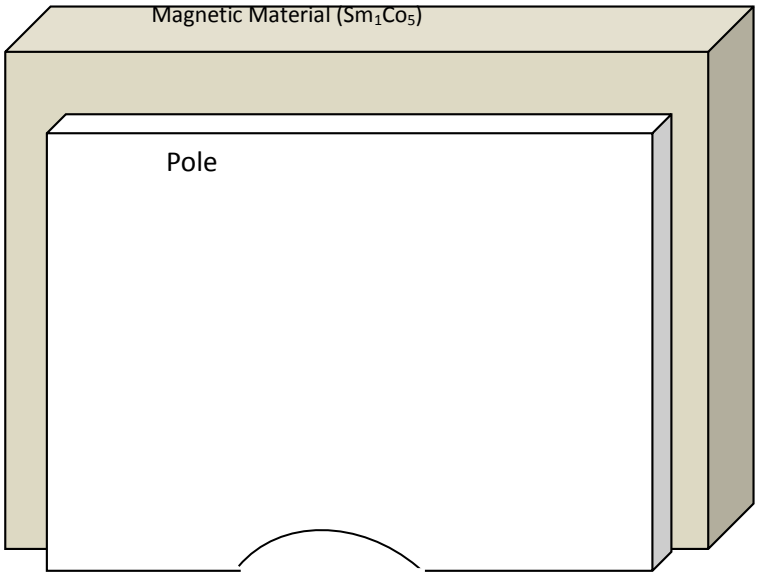

Figure 9: Half period of the CSU undulator showing curved pole face (near the bottom) [15].

Table 2: Undulator Design Parameters [mm]		
Undulator Wavelength	λ_u	25.0
Half Gap	h_s	4.0
Overhang of magnet	O	6.0
Half thickness of pole	D_2	2.0
Half thickness of magnet	h_2	4.25
Height of pole	D_3	40.0
Height of magnet	h_3	45.0
Half width of pole	D_1	15.0
Half width of magnet	h_1	21.0

The CSU system is designed for use as an FEL in the terahertz (THz) regime. To achieve THz radiation, the wavelength of emission, λ', must be between 0.1-1mm. From Table 1, the kinetic energy (KE) of the linac is 6 MeV. However, to obtain good emittance of the beam, only 5 MeV will be generated, corresponding to a relativistic gamma of:

$$KE = (\gamma - 1) * m_0 c^2 = 5MeV = (\gamma - 1) * (0.511MeV) \rightarrow \gamma = 10.8$$

The equation to find the wavelength of emitted radiation from Equation 3 is:

$$\lambda' = \frac{\lambda_u}{2\gamma^2}(1 + K/2^2) = \frac{0.025m}{2 * (10.8)^2}(1 + 1^2) = 215\mu m$$

This corresponds to a frequency of $f = \frac{c}{f} = 1.39$ THz.

When the FEL was operational at the University of Twente, the measured wavelength of light was $\lambda = 252.2\mu m$, for a frequency during the pulse of 1.57 THz [19]. These experimental results are on the same order as the values calculated above, verifying operation in the THz regime.

PULSED-WIRE SYSTEM DETAILS

Setup

The pulsed-wire technique requires a few key elements to function. These include a pulse generator, laser and photo-detector system, a wire, pulley and weight, a way to accurately position the wire, and a data acquisition system. This chapter explores the various designs and equipment used as well as the procedures involved. The entire life cycle of the project will be discussed, from preliminary concepts to the completed product. Much of the design was built from scratch and fabricated in-house. Two intern students, Josh Smith and Jon Hoffman, created some of the procedures and circuits in the summer of 2014 under the author's guidance.

Pulse Generation

Obviously an important part of the pulsed-wire method is the generation of the actual pulse delivered to the wire. The circuit needs to provide enough current amplitude for the photodetector and oscilloscope to detect the displacement of the wire over the noise level. For a magnetic field of 0.61 T, such as the CSU undulator, the amplitude of the pulse must be over 1 A. Such a current pulse and field would displace the wire by 4.13 μm. In our setup and photodiode gain levels, 1 μm of wire displacement corresponds to a 0.13 V change on the oscilloscope, and the signal is easily detected over noise.

To measure the first field integral a power amplifier circuit capable of providing a short, 20 us, square current (1 A) pulse with short rise and fall times was developed. The circuit was actually designed and built as an undergraduate design project at CSU and the schematic is

shown in Figure 10. Later, it was optimized and a second circuit was added capable of creating a high-quality long, ~ms, pulses.

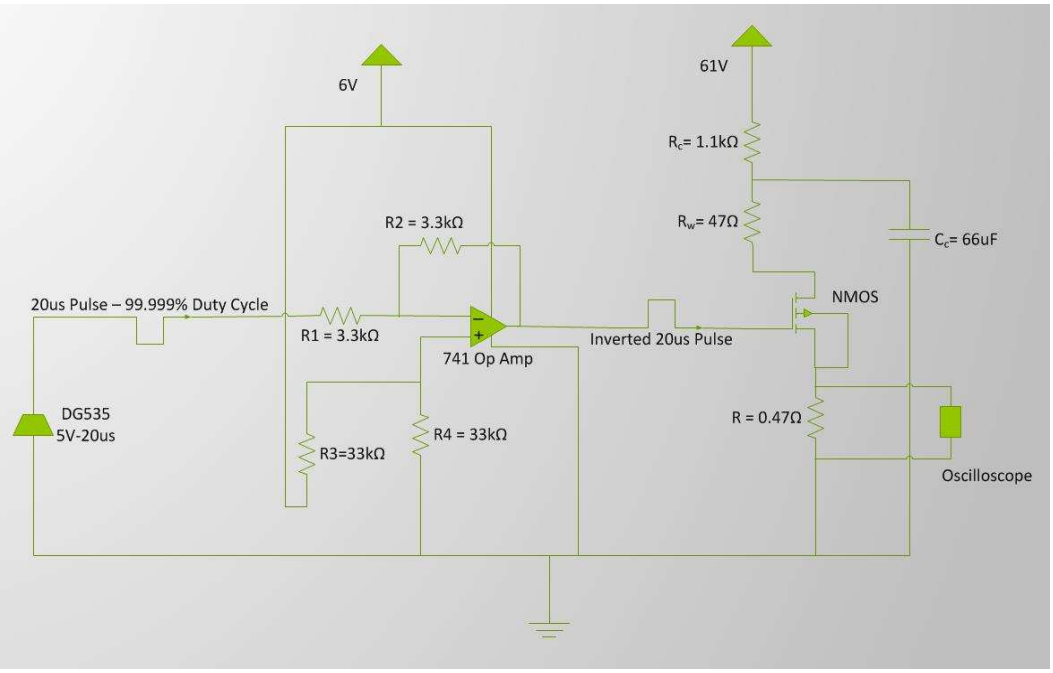

Figure 10: Schematic of the pulsing circuit. The 47 ohm resistor is the wire load.

The circuit utilizes the precise timing of a DG535 pulse generator, capable of producing 4V square waves into a 50 Ohm load with a duty cycle of 99.998% at the desired repetition rate, 1Hz. This wave passes through an inverting 741 op-amp with a gain of -1, creating a 4 V pulse with a width of 20 µs. The pulse subsequently arrives and triggers a high voltage NMOS transistor to turn “on.” At the source terminal of the MOSFET is a large capacitor bank, charge to 61 V, and the charges are dumped while the MOSFET is “on” until the 20 µs pulses passes and the transistor turns “off.” There is a current limiting resistor between the capacitors and power supply for protection of the capacitor charging circuit. The current passing through the

MOSFET also must pass through the BeCu wire (the resistor marked R_w) and also passes through a small resistor at the drain used for measurement with an oscilloscope of the signal. The RC time constant, consisting of the capacitance and resistance values of the circuit, is important for decent pulse shapes. Depending on the length of the pulse, long or short, a different RC circuit is used for its specific time constant, τ. A shorter time constant diminishes the rise and fall times of the pulse, but can't sustain a long pulse due to the quicker draining of the capacitor. The short pulse is shown in Figure 11.

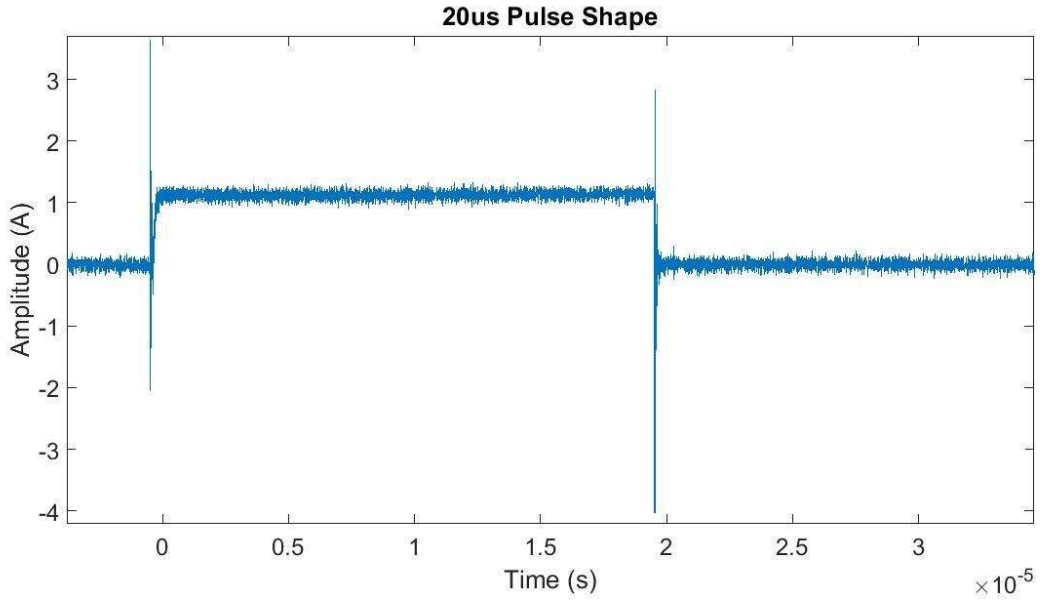

Figure 11: The short current pulse; 20µs.

In Figure 11, large turn on and turn off transients can be seen. This circuit was hand soldered by the author as well as another student without much experience. I believe the transients come from parasitic capacitances and inductances in the circuit caused by the electrical pulse from the switch. These parasitic effects most likely come from imperfect

soldering and resonate at their characteristic frequency. This ringing of unwanted current has some detrimental effects on the pulsed-wire measurements and will be discussed further in the "System Difficulties" section of this paper.

A longer time constant has worse rise and fall times but is capable of creating quality millisecond pulses. The circuit was designed with a switch to choose whichever RC circuit is desired for the different pulse lengths. The shape of a 12ms pulse is shown in Figure 12.

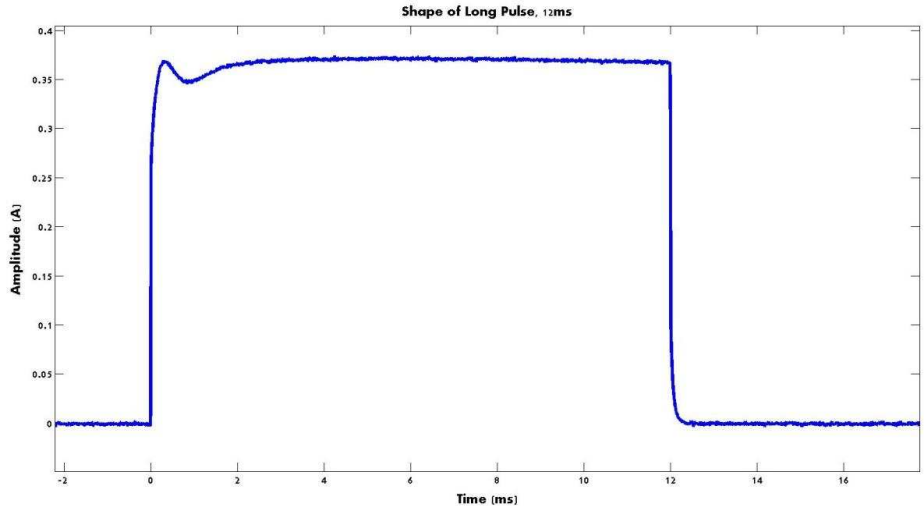

Figure 12: The long current pulse; 12ms.

Laser/Photo-Detector

This section describes the laser, slit and photodetector system used to detect the motion of the pulsed wire. A 635 nm fiber laser is used with an amplified Si photodetector. A thin, 40-µm slit is placed over the photo-detector and aligned, using a precision cage rotation stage, parallel to the wire's axis. The wire is placed between the collimated laser and the slit and is positioned such that the wire, as shown in Figure 13 covers half the slit. This is done by mounting the photodetector onto a differential 1" translation stage and moving it so that the

wire passes completely over it. The oscilloscope will show a constant reduction in voltage, or laser light being detected, as the wire covers more of the slit.

Figure 13: The wire positioned over the slit.

A documented procedure for positioning the wire over the slit is important for creating reproducible results. Having reproducible results is important in finding the magnetic center of the undulator, described in a later section. First, the voltage is documented in the lab notebook when the wire is completely off of the slit, the maximum signal being detected. When the wire is completely covering the slit, a small signal is still detected due to refraction of the laser light from the wire, and the minimum voltage value is noted. The difference between these minimum and maximum values is calculated and the detector is positioned such that half the slit is covered by the wire, or the signal voltage is halfway between the noted maximum and minimum values. By placing the wire halfway over the slit, it allows for the largest amplitude of

deflections that can be detected before saturation. Saturation occurs when the wire is completely off the slit and larger movements of the wire cannot be detected.

Presets on the oscilloscope were utilized to obtain even more accuracy from this method. The value of the signal with the wire covering half the slit was offset to zero on the vertical axis of the oscilloscope, such that when the wire is at the correct position, the signal is in the center of the screen. Utilizing this process saved a great deal of time attempting to center the wire over the slit before every measurement.

Wire Positioning

Precise positioning of the wire within the undulator is a major requirement of the pulsed-wire method. Further, because our undulator has electron beam focusing properties in both directions finding the center is critical to ensure that measurements are done at a location where the beam is supposed to be. Also, the measurements will be used in the fiducialization process required in the survey procedure to locate the undulator precisely into the beamline.

This section describes the different methods tested to accurately position the wire. All of the methods utilized an x,y translation stage apparatus, with 0.001” resolution, connected to a vertically positioned structural rail, as in Figure 14. Two of these positioning stages were placed at either end of the pulsed-wire setup.

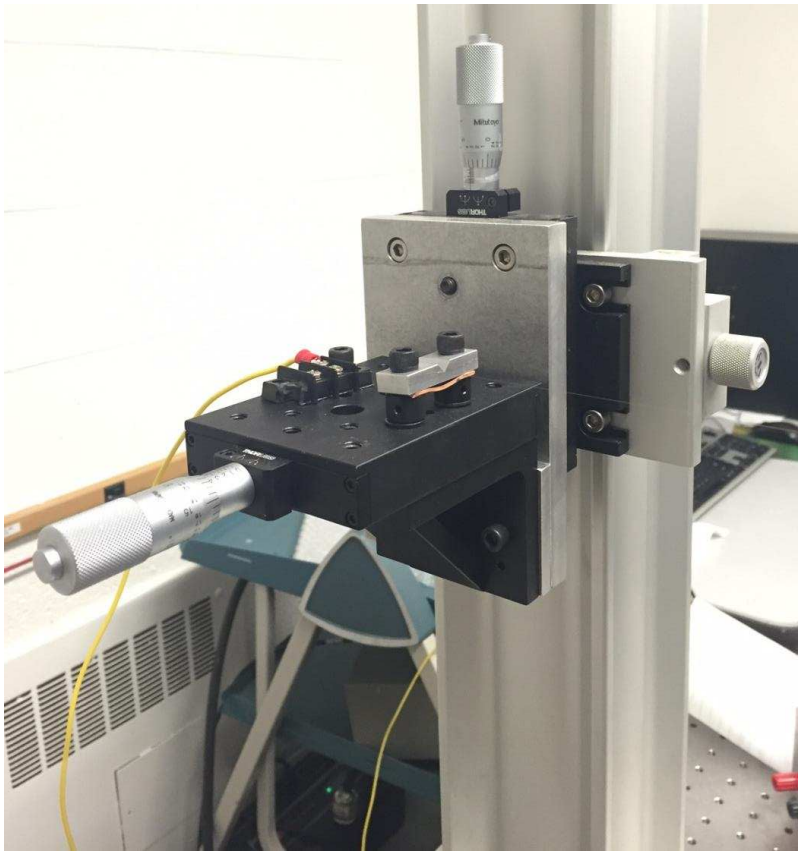

Figure 14: Wire positioning system.

The first positioning method developed involved using a laser, with a 100-µm spot size, to ablate holes in brass disks. These brass disks were inserted in 1” optical mounts and placed inside locking optical holders, shown in Figure 15. These were mounted, perpendicular to the wire’s axis, on x,y translation stages. Using a high resolution microscope, the brass disks were then inspected. Focusing on the ablated holes, non-uniformity in shape and differences in the size of the holes, ranging from 100-300 µm, were found. The major accuracy issues discovered were too great for the disks to be used in the setup.

Figure 15: Laser ablated holes in a brass disk for wire positioning.

For more precise positioning of the wire, the “V-blocks” shown in Figure 16 were developed. These were machined from aluminum by the CSU machine shop. The tensioned wire was moved back and forth to be sure it settled in the bottom of the cradle. The V-blocks were mounted to x,y translation stages with electrically isolated bolts to prevent grounding of the wire. The wire was moved in the plus and minus direction in both the vertical and horizontal planes to check for any slipping of the wire in the cradle. This design was verified when there was no noticeable movement of the wire in the bottom of the “V.” Thus, the accuracy of the location of the wire is based solely on the resolution of the x,y translation stages; 0.001” (25 μm).

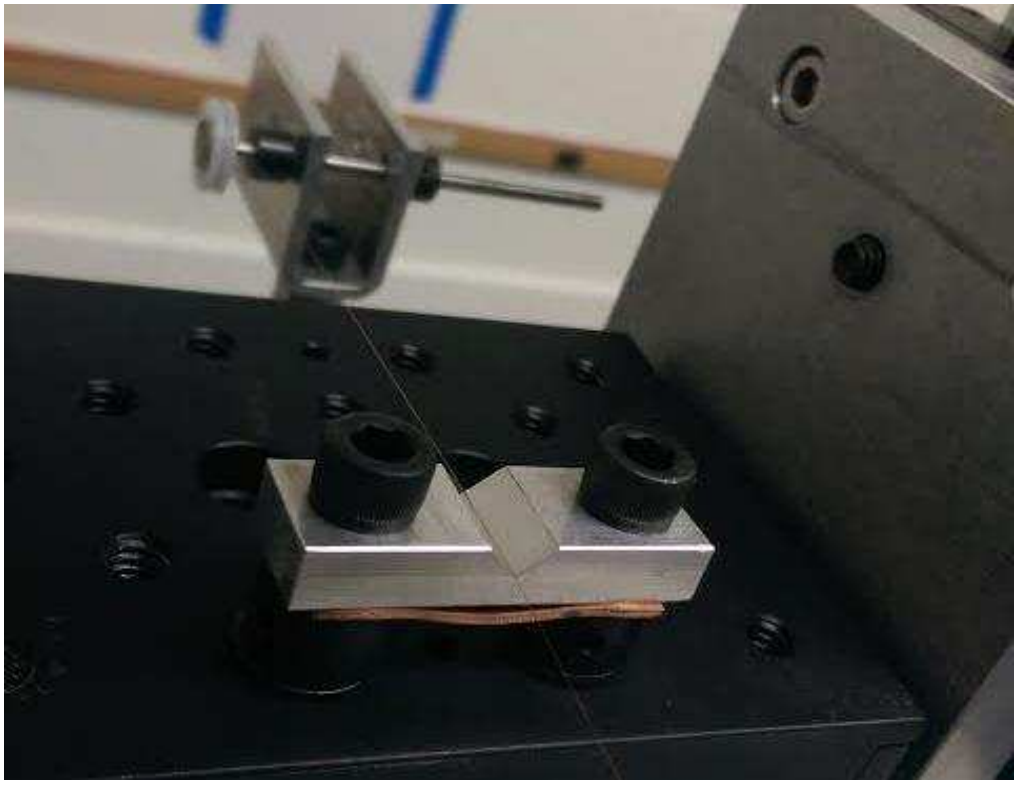

Figure 16: V-Blocks for precise wire placement within the undulator.

Tension

The pulley and weight, shown in Figure 17, have two main functions in the pulsed wire setup. First, the tensioned wire and pulley dampen the reflections of the pulse within the wire. One pulse must dissipate before the next pulse can be introduced. Faster dissipations of the reflections lead to a higher possible repetition rate of the signal. The tension on the wire also assists with dispersion issues. Increased wire tension reduces dispersive effects. Thus, the wire tension, initially at 0.431 N, was increased to 2 N. The reduction in dispersion effects from increased weight can be seen in Figure 18.

Figure 17: Pulley and weight for tensioning of the wire.

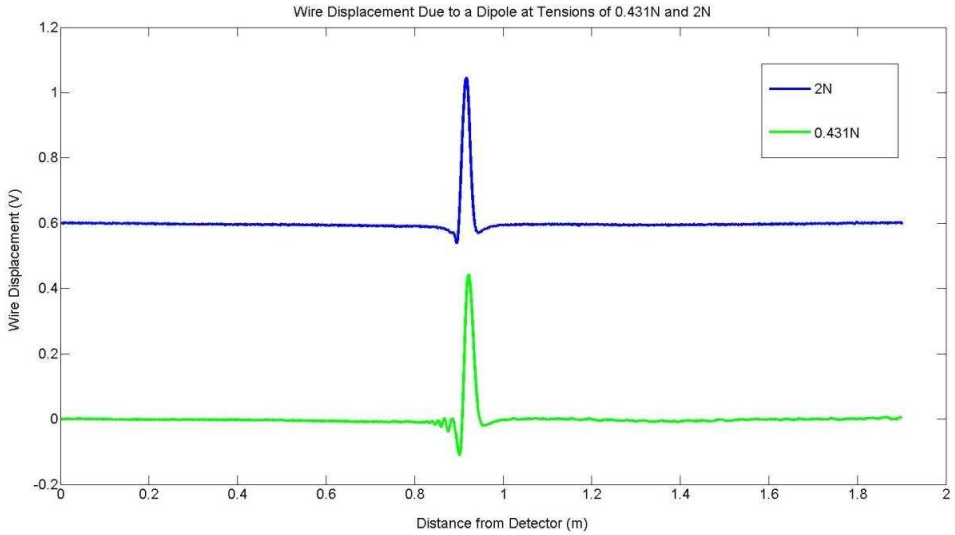

Figure 18: Difference in dispersive effects with increased tension in the wire.

Procedures

Reference Magnet Measurement

The pulsed-wire measurements of the undulator field do not provide an absolute measurement of the field and so must be calibrated. This can be done with a Gauss meter and an easily measured reference magnet. Once an accurate absolute measurement of the reference magnet is made it can be measured simultaneous with the undulator magnet thus establishing the overall absolute scale of the pulsed-wire measurement.

A reference magnet with field strength similar to the undulator was desired so that the wire displacement due to the magnetic field could be seen on the oscilloscope at the same scale. Many concepts for this reference field were developed, including electromagnet designs and using a single permanent magnet acting as a dipole. Ultimately, two high-field permanent magnet dipoles were put together with alternating field directions to simulate one period of the undulator. The reference magnet is shown in Figure 19.

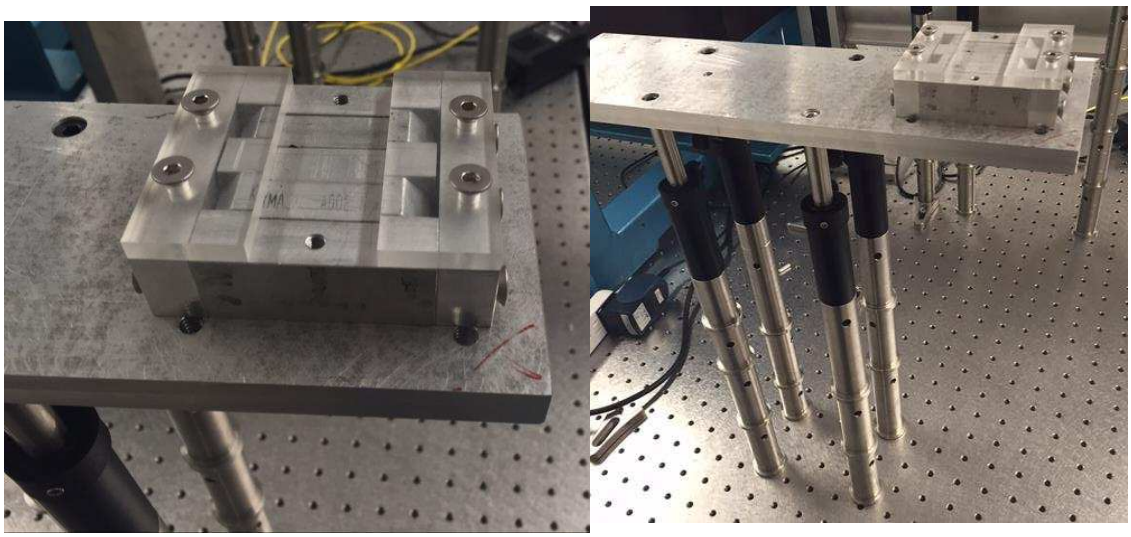

Figure 19: The final reference magnet designed with two high field permanent magnets.

The measurement process for mapping the magnetic field of the reference magnet consisted of a Gauss meter used in conjunction with a Hall probe. The probe itself was mounted on a 24” translation stage with movement in a direction parallel to where the wire’s axis would later be (z-axis). The probe was also mounted to both vertical (y-axis) and horizontal (x-axis) translation stages. This setup can be seen in Figure 20. Measurements were taken at an interval of 0.5” until the field could be detected, then measurements were changed to 0.1”. Once this base measurement was taken, with the Hall probe near the magnet face (2 cm), the probe was raised and measurements were taken at different heights above the magnet. All measurements were taken at the exact same locations along the z-axis.

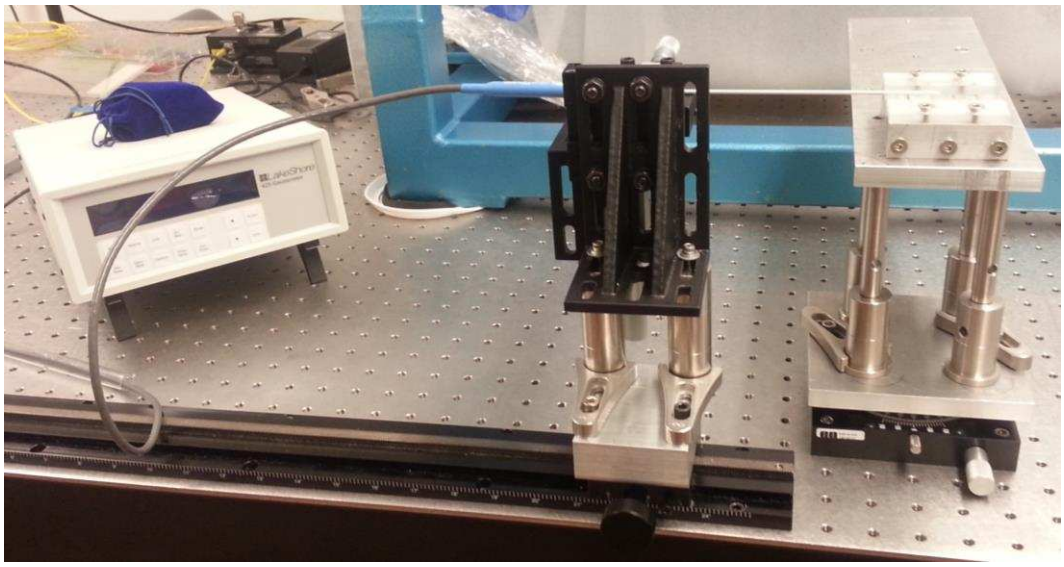

Figure 20: The Hall probe and Gauss meter setup for reference magnet measurement.

Next, the hall probe was set at a height of 5 cm and mounted on a 360 degree rotational translation stage. The 0 degree position corresponded to the angle directly down the z-axis.

Measurements were taken at various angles from the z-axis in both the vertical and horizontal directions. The results of the Hall probe measurements can be seen in Figure 21.

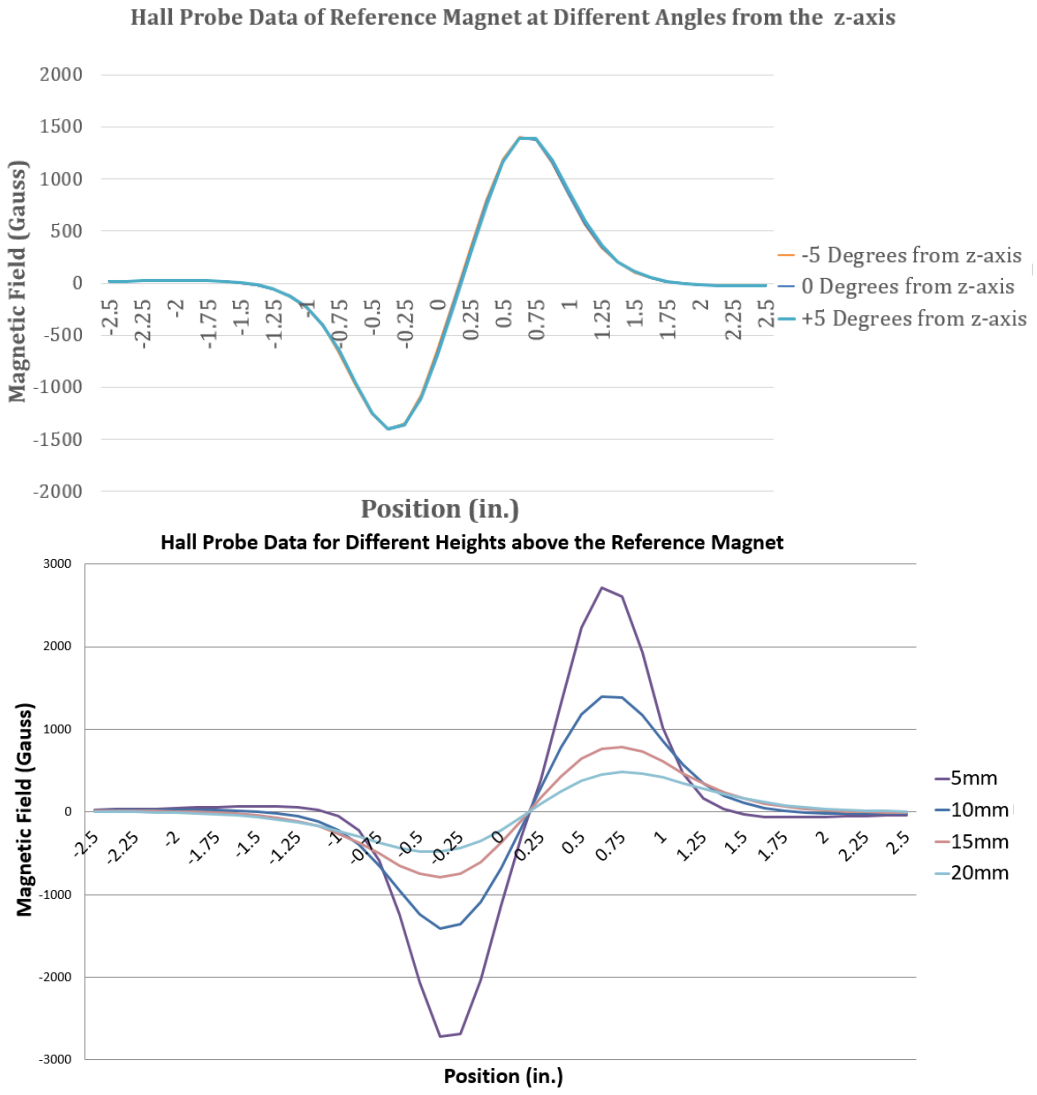

Figure 21: Hall probe data for the reference magnet at various angles (top) and heights above the magnet surface (bottom).

The results show an obvious inverse correlation between the height of the measurement above the magnet's face and the strength of the magnetic field. The quality of the measurements degrade above 10 mm, so the final wire height will need to be below this. One can also see that an angle between $-5° < \theta < 5°$ had no noticeable impact on the field profile. The difference in field within these angles are at a level below the resolution of the detection system. This gives us confidence that the wire itself can be setup and aligned in a way such that and residual angle has no impact on the measurement.

The next step was to actually take pulsed-wire measurements. The measurements could then be compared to the Hall data to generate an absolute scale for further measurements with the pulsed-wire system.

Measurement Process/Data Acquisition

Data acquisition is a key area of the pulsed-wire process. A Tektronix TDS 3054b oscilloscope was used for this purpose. The oscilloscope has network connectivity via an Ethernet cable for direct downloading of measurements to the computer. With a sample rate of 5 GS/s, the horizontal (time) resolution is more than sufficient. The oscilloscope starts sampling via an external trigger, which is connected to the DG535. The start of the pulse, rising edge, triggers the oscilloscope to begin to take data. The horizontal axis was set to measure the signal clearly, without any reflections being measured, so a 10-ms window was used. The vertical window (voltage) is set differently depending on the pulse length. To reduce signal noise, averaging was used on the oscilloscope. For accuracy, 512 samples were averaged, the oscilloscope's maximum capability. Limitations of the oscilloscope are discussed in a later section.

Finding the Center of the Undulator

Determining the center, specifically the magnetic center, of the undulator is important. To accurately simulate the electron beam, the wire must be precisely in the magnetic center of the undulator. Thus, a method needed to be developed to accomplish this.

The obvious starting place was to locate the mechanical center of the undulator and move on from there. Finding the mechanical center is relatively straightforward as the design parameters of the magnet are stated; see table 2. Once the mechanical center was found, fiducialization marks could be placed on the undulator to easily find the exact point again in the future. The magnetic center could then be found based off the mechanical center and noted for future reference.

Mechanical Center

The design of the undulator was such that the physical center of the undulator should also be the magnetic center of the field [10]. The original thought was that very small changes in the wire's position in the undulator gap, around 1 mm, would cause large changes in the displacement of the wire due to increasing magnetic field strength. Therefore, the goal was to position the wire to within 100 μm of the geometric center on either axis while keeping the process as simple and easy to recreate as possible. Many different methods were contemplated and tested before determining one that provided accurate and consistent results.

First, a "crosshair" method was tested. This idea came from J.W.J. Vershuur as a possible method that was originally used at the University of Twente. This design consisted of wrapping fishing line in a figure-eight pattern around four screws that protruded from the

screw holes used for connecting the undulator to the vacuum system of the beamline. The center point, where the wires cross, should be the mechanical center of the undulator. The next step was to position the copper beryllium wire as close to the center point as possible. Since the crosshairs were sitting at a 45° angle to the ground, it was very difficult to observe whether the wire was touching just off center and sliding along the fishing line to the center point or not. Trying to prevent this from happening, the wire was first leveled by eye and then moved horizontally into the center. A magnifying glass and later surveying equipment were used to try and determine the point when the wire just touched the crosshair, as in Figure 22.

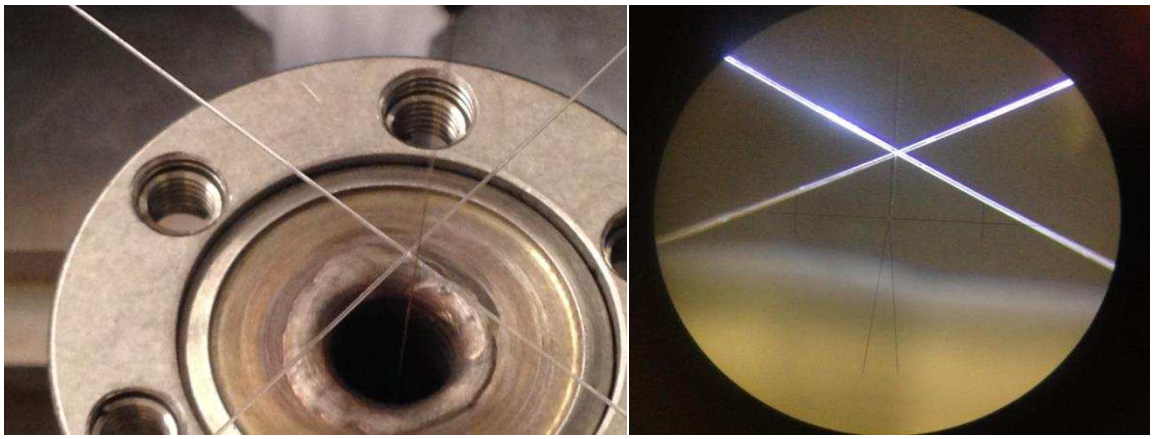

Figure 22: Different views of the crosshair method.

Once the wire was barely touching, the fishing line was removed and the wire was moved towards the center by half of the fishing line's thickness, around 50µm. However, there were some insurmountable issues that arose with this method. First, the point where the wire just touched the fishing line was almost impossible to observe, even with the surveying

equipment. Second, there was no documentation that actually described the screw holes as being some distance from the center of the undulator. This greatly reduced the confidence in the accuracy of the results so another method needed to be implemented.

The next method involved using the surveying equipment, as seen in Figure 23. First, the scope was focused on one end of the undulator, where the pole profiles can be seen clearly. The scope can be tilted upward and downward with precise angle measurement. The angle above the horizontal at the location of the bottom of the undulator's top pole was noted. Then, the angle at the location of the top of the bottom pole was found. The location in between the two angles was the physical center in the vertical axis. The wire could then be raised or lowered to align with the scope's crosshairs at this location. Due to the unknown angle of the undulator's axis from the table, the wire needed to be aligned on both sides and rechecked after any movement. The reproducibility of this method was very good and the surveying equipment was simple to setup and use. However, the scope had fine angle measurement capabilities on the vertical axis, but not on the horizontal. It was impossible to utilize this method to find the horizontal center.

Figure 23: Josh using the survey equipment to verify the position of the wire.

The method that was ultimately used to find the horizontal center was a combination of different ideas that had been developed. First, two translation stages with micron resolution were combined with an angle bracket and aligned in the vertical and horizontal axis. A third smaller translation stage in the longitudinal axis was attached with an ohmmeter probe locked onto it. This gave accurate movement in all needed directions. A simplified version of the setup is shown in Figure 24, without the vertical stage. The entire setup was placed on a fourth translation stage, with 24” of movement in the longitudinal direction. This allowed for the entire apparatus to be moved in and out of the undulator opening efficiently. To find the horizontal center, the test probe was moved along the horizontal axis to the point where the

conductive pole meets the non-conductive aluminum plate. The other ohmmeter probe was held on the conductive pole. When the tip of the test probe alternated between the conductive and non-conductive sections, the ohmmeter would switch between having a valid resistance value as an output and having infinite resistance. When the circuit was open, or the test probe was touching the aluminum, the ohmmeter would emit a beeping noise. The location of the edge of the pole was documented and repeated for the other edge of the pole. The difference between the two measurements was halved, giving the horizontal center of the pole and undulator.

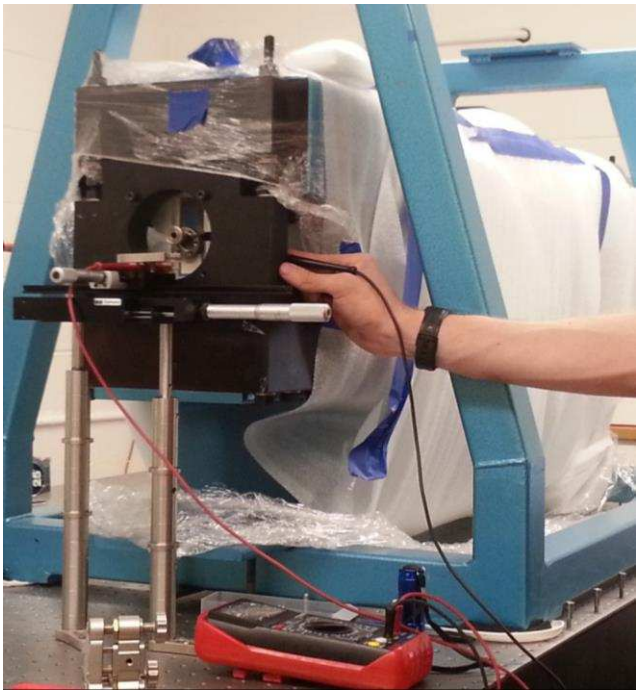

Figure 24: Simplified version of the method to find and mark the geometric center of the undulator.

The probe was then used to physically marked the center. The probe was positioned to the calculated horizontal center and the probe tip moved in the longitudinal direction towards a piece of tape that was placed on the undulator where it would slowly punch a hole. This created a visible mark that could be used in conjunction with the survey scope to position the wire. The process was repeated a few times to create a series of “dots” in a line as seen in Figure 25, above and below the gap of the undulator. This helped to both verify that the method was consistent and also provided an easy way to center the wire in the future by creating permanent fiducialization marks. This method is easily the most accurate and reproducible method that was used and should therefore be replicated in the future if the center needs to be found again.

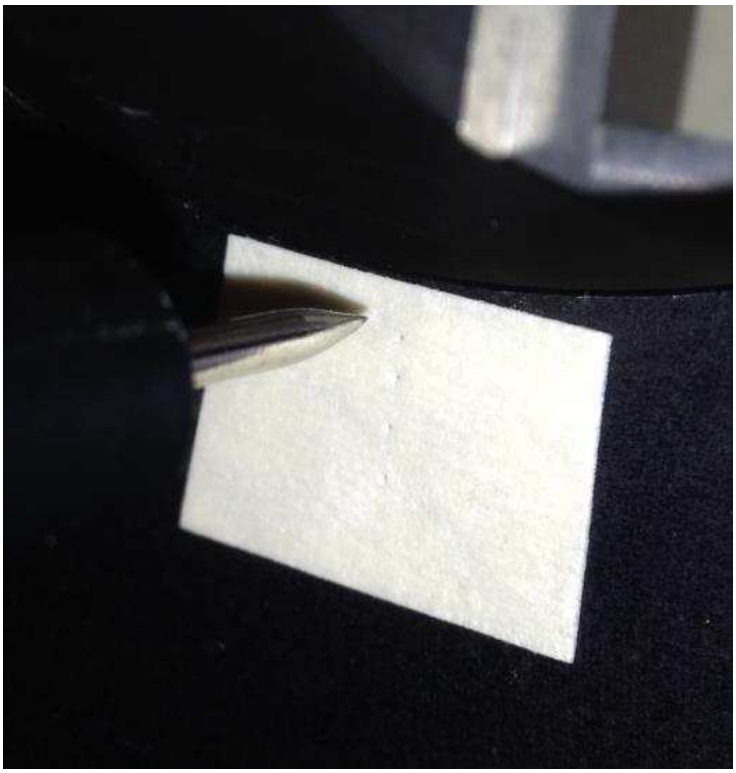

Figure 25: Fiducialization marks being placed with a probe onto the undulator.

As stated earlier, noise issues have been the major limiting factor in this project's accuracy. Most issues were overcome throughout the lifecycle of this project. However, ground vibrations at 60Hz are still slightly apparent in the measurements, with amplitude around 30 mV. (We suspect these are coming from the synchronous pumps used in the adjacent hydrology lab.) Using the oscilloscope and averaging helped to reduce this effect to around 5 mV, but it was not eliminated completely. The final limitation of this project was the 9-bit vertical resolution of the oscilloscope. It was determined that the resolution should be at least 12-bits to more accurately discriminate different signals in order to find the magnetic center and make sufficient assumptions about the fields in the undulator.

Magnetic Center

As stated earlier, the wire needs to be aligned as close to the magnetic center of the undulator as possible to accurately simulate the electron bunch. The undulator was designed with a parabolic pole shape, and thus has a field strength profile that is quadratic in strength such that the minimum peak field resides in the horizontal center of the undulator along the undulator axis. As will be demonstrated later, the differences in magnetic field strengths within 1 mm of the magnetic center are small. Interpolating the data far away from the center and with the knowledge that the field is quadratic, the center can be found with relatively high confidence.

To determine the magnetic center of the undulator, the wire was first placed onto the mechanical center (described later). Measurements were then taken at different locations across the gap of the undulator in both the x- and y- directions. To see the peak fields at the different locations, the root-mean-squared (RMS) value of each measurement was taken. These

RMS values are plotted against the wire's position in the gap. As seen in Figure 26 the peak magnetic field changes when the wire is placed in different locations within the undulator gap. To eliminate noise issues in the peak field measurements, a high-pass filter was used. Any effect the filter had on the data was constant over every measurement taken. Thus, the filter was helpful for finding the peak fields, but is not an accurate representation of the actual field integrals.

Alignment of the wire directly along the axis of the undulator with no angle was important for precise measurements. A solid method for aligning the wire was determined by looking at the field profiles of the wire at different locations across the gap. Misalignment of the wire (not parallel to the undulator axis) is a problem for accurate measurements. Two pulsed-wire measurements are needed to witness any wire misalignment. If the wire is parallel to the undulator axis, the two measurements will have an amplitude difference that is constant. If the wire is misaligned, the difference in amplitude will not be constant. One may have a larger amplitude at the entrance of the undulator and smaller amplitude at the exit. This is due to a combination of the parabolic field profile as a function of horizontal position and an undesired yawing of the wire with respect to the true undulator field axis.

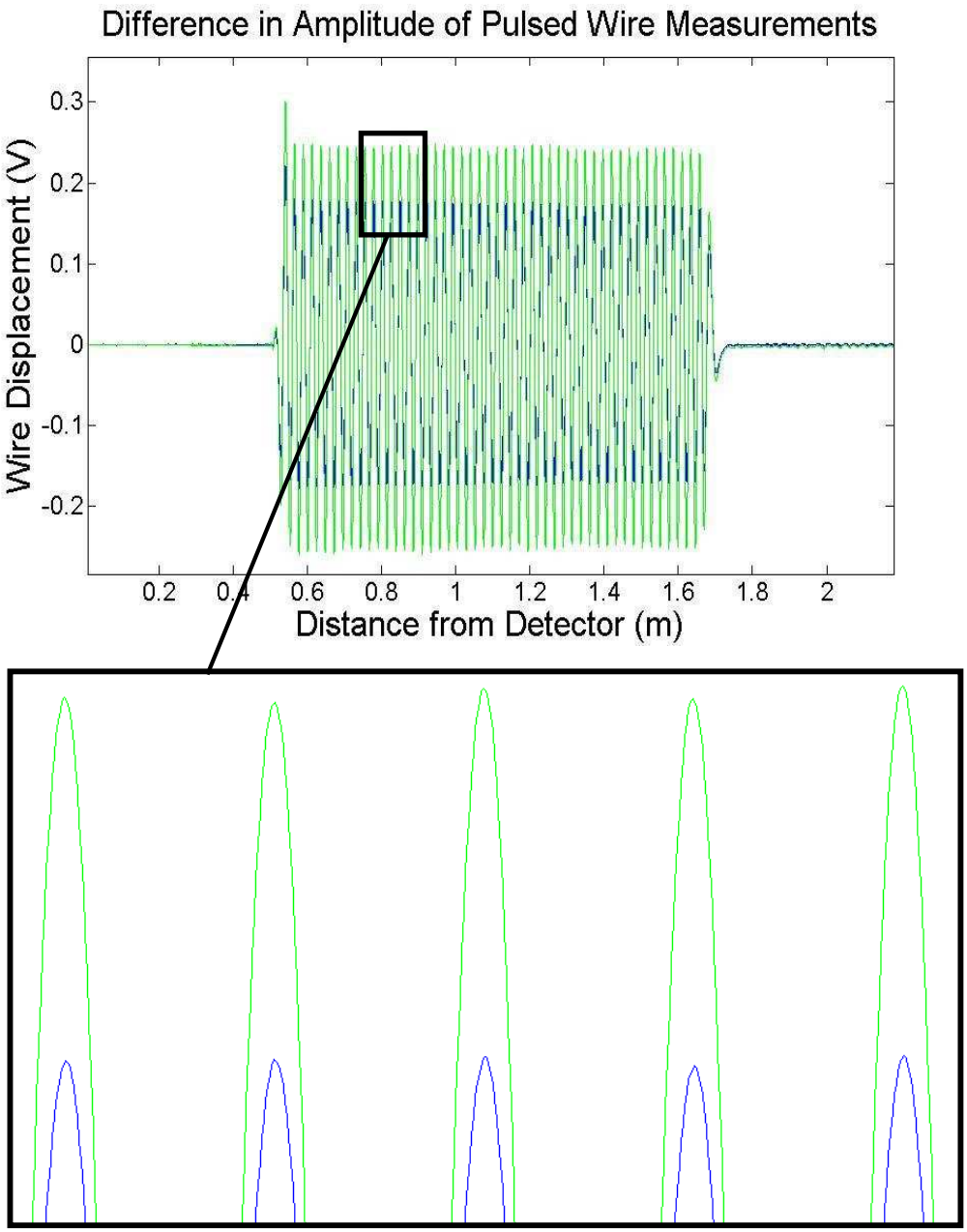

Figure 26: The difference in displacement (magnetic field) amplitudes for locations closer and further from the magnetic center of the undulator. The smaller amplitude corresponds to a location closer to the magnetic center. Also seen is a zoom of a specific section of the plot.

We performed the following process to determine the magnetic center of the wire with respect to the mechanical center. Using the mechanical center as the reference axis the wire was moved +/- 3 mm in the x- and y-planes in increments of 0.025 inches (0.635mm) while at the same time measuring the RMS field. The RMS value of the peaks of the oscillations within the undulator for given locations in the gap are shown in Figure 27, with the zero point being the mechanical center. Analysis of the data using fit parameters gives a high confidence result for the location of the magnetic center, within tens of μm. The hypothesis that the mechanical center and the magnetic center being at the same location is correct. Thus, the wire only needs to be aligned in the already marked mechanical center before measurements are taken. This greatly reduces setup time and effort.

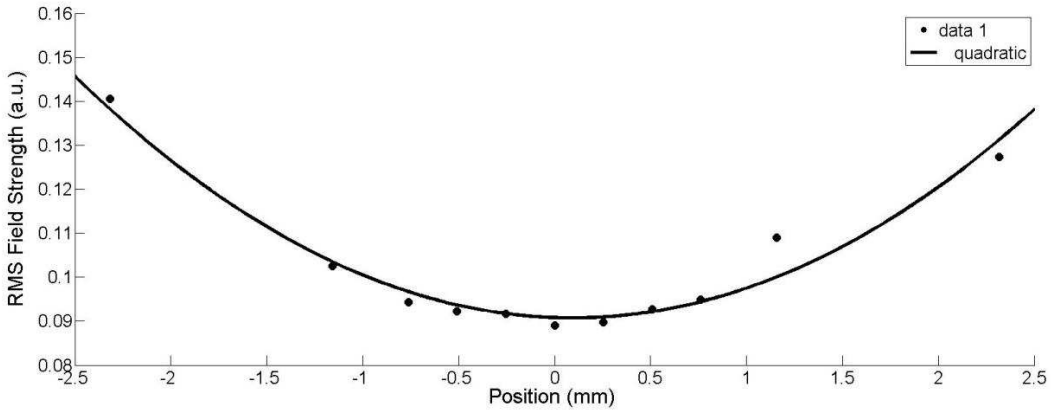

Figure 27: RMS field strength of the undulator at specific locations away from the geometric center of the undulator with a quadratic fit added.

Final Results

Wave Speed

As stated earlier, the wave speed in the wire is a function of frequency and follows the Euler-Bernoulli equation. The theoretical value for the wave speed should follow equation 18; $c(\kappa) = c_0\sqrt{1 + \frac{EI_w}{T}\kappa^2}$. However, due to errors in manufacturing, an experimental method was implemented to find the correct values of c_0 and EI_w. By taking two measurements with the pulsed-wire method, one with the reference field close to the detector and another displaced 30cm away, one can find the experimental value for the wave speed and the coefficient of the quadratic term. The raw data of the two signals, overlapped for comparison, can be seen in Figure 28.

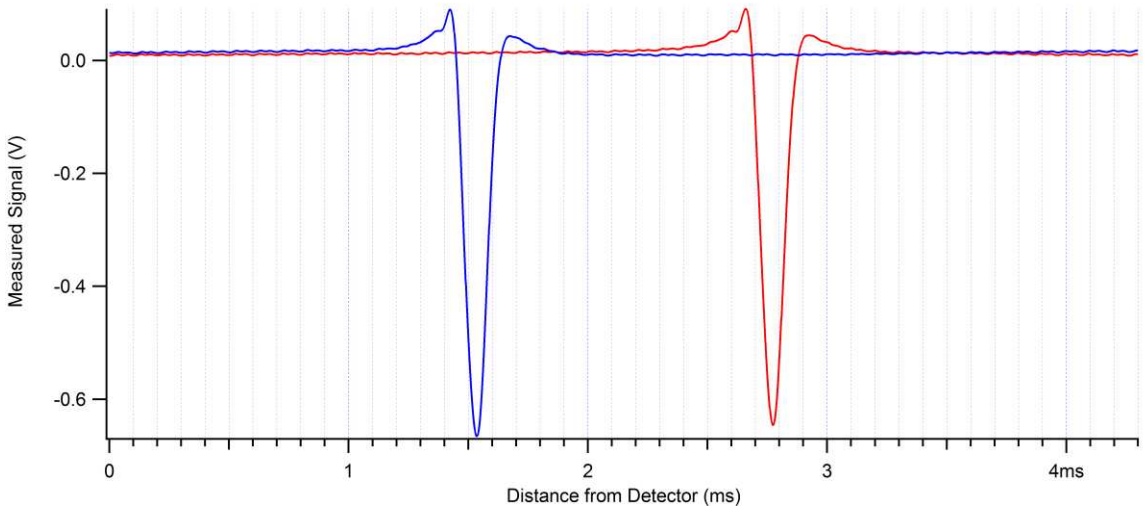

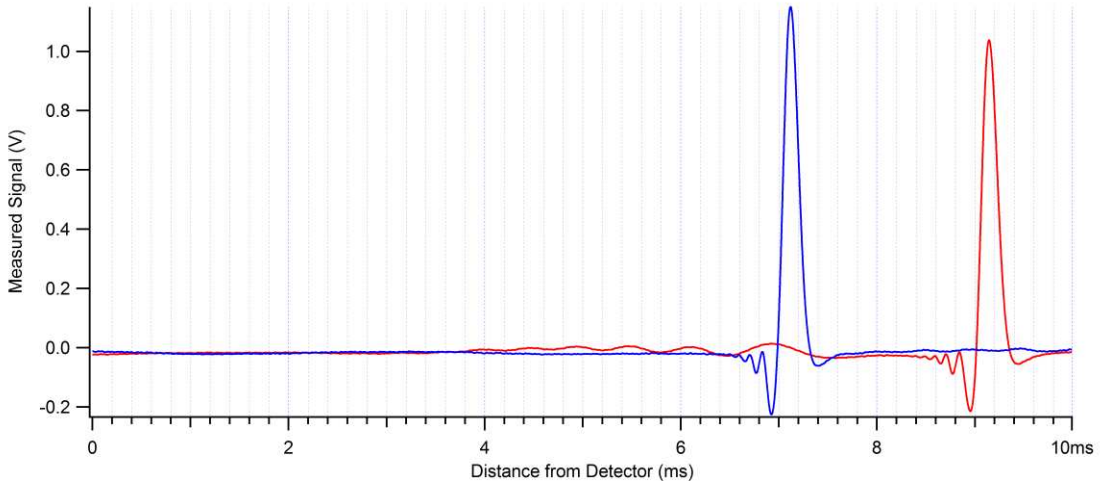

Figure 28: Reference Magnet measurements taken 30 cm from each other used to calculate the dispersive wave speed in the wire; 2.3N (top) and 0.85N (bottom).

One can now determine the FFT of both the original and displaced measurements (Figure 29). It is important to dissect this data because it will show the frequency components that are contained in the signal. We can then make a more accurate fit of the wave speed because frequencies not contained in the signal are just noise and do not need to be fit to.

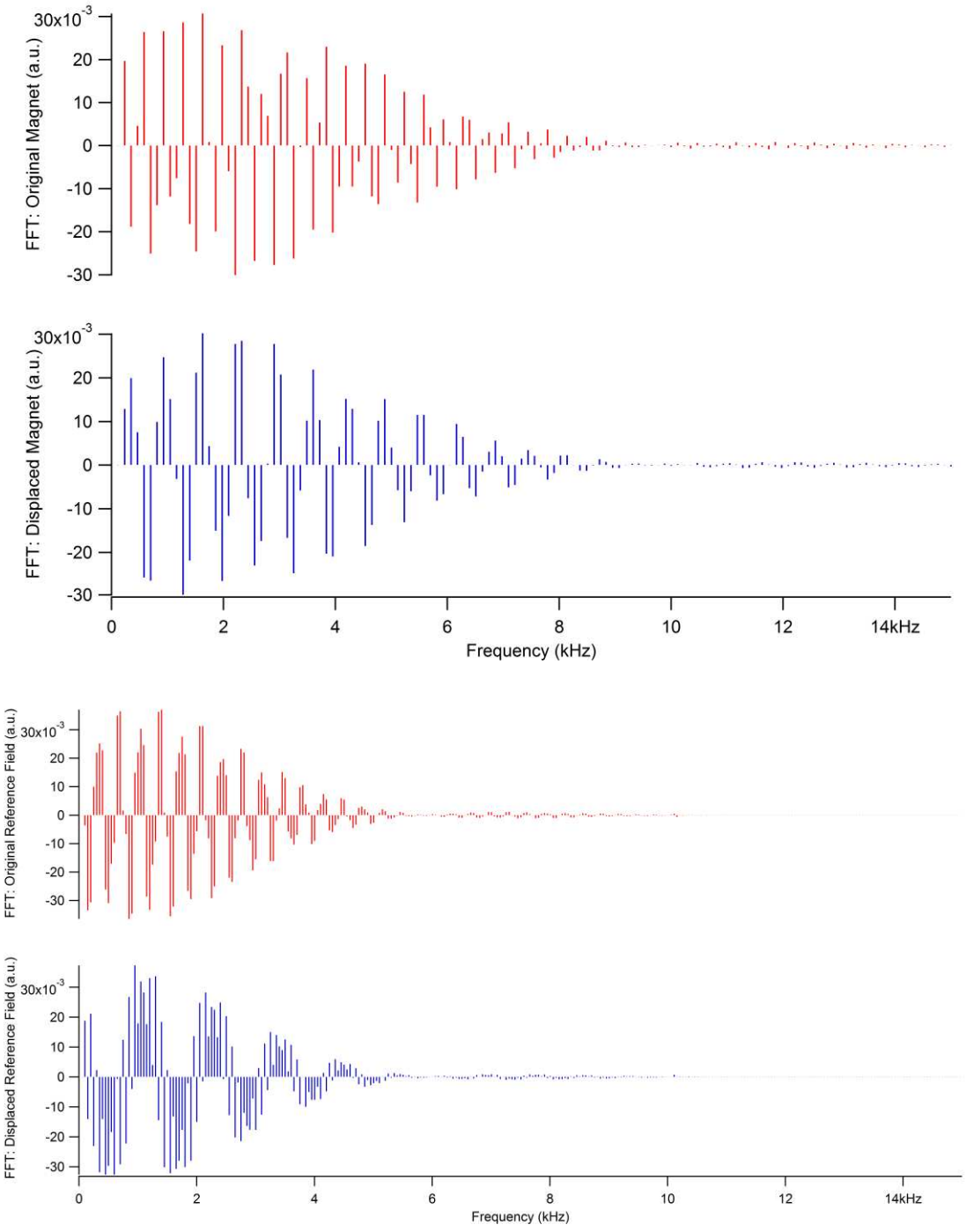

Figure 29: FFTs of the measured signals; 2.3N (top) and 0.85N (bottom).

In Figure 29, it can be seen that the maximum frequency components in both tension schemes is around 10 kHz. A more accurate wave speed curve can be obtained from a signal

with higher frequency components. Some ideas are presented to accomplish this in a later section.

Determining the wave speed was accomplished by implementing equations 17 and 19 into a Matlab script. Analyzing the phase of the result from equation 17 and using this phase in equation 19 allowed for the determination of the wave speeds in the wire. The results can be seen in Figure 30 and is compared to the theoretical value of the wave speed as described above.

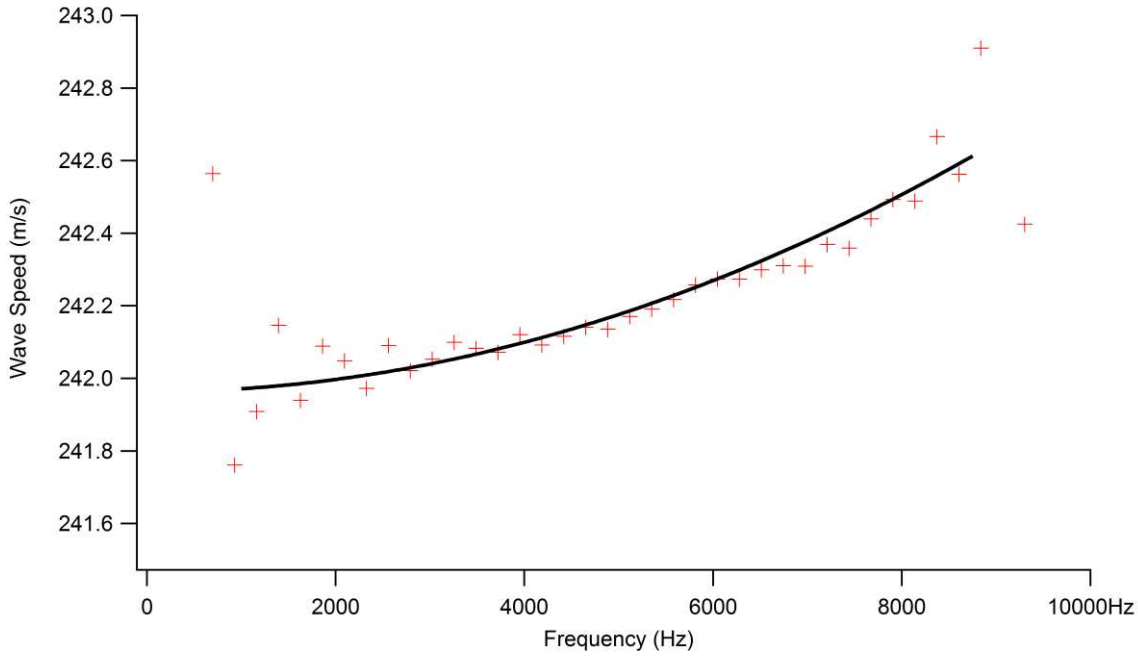

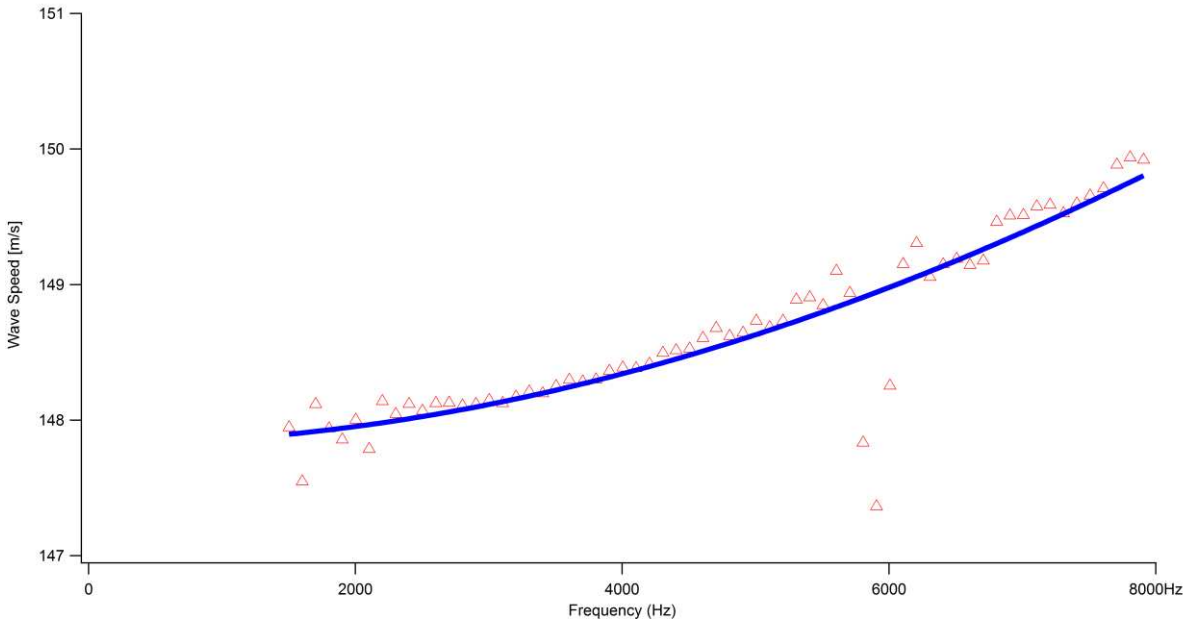

Figure 30: Wave speed determination from two measurements, 30cm apart; 2.3N (top) and 0.85N (bottom).

From the figure 30, one can see that for higher frequencies, above 2kHz, the experimental results follow the theoretical fit extremely well. However, at lower frequencies, the two graphs differ wildly. This is due to major low frequency noise issues and equipment limitations that will be explained later. In figure 30 (bottom), a dip in the wave speed occurs at ~6 kHz. To understand this, we see that the full width of the pulse is approximately 1.5×10^{-4} s. This corresponds to a frequency of $f = \frac{1}{1.5 \times 10^{-4}\, s} = 6.7\ kHz$. The signal is only a single pulse so there should be a modulation of the signal from the effective window. The pulse can be thought of as a perfect sine wave that is modulated with a square wave window with amplitude 1 and duration 1.5×10^{-4} s. The two together, the perfect sine wave and the square pulse window, would then make a single positive pulse. If the FFT of that combination is taken, you

get a signal that is modulated by a $\frac{sin(x)}{x}$ term where the first zero of the sinc function is at around 6 kHz.

The experimental results for the wave speed parameters (Eq. 18) are shown below for the two different tensions. The errors shown are within ±1 standard deviation and show that the fit is very accurate and a strong representation of the data.

Table 3: Wave Speed Parameters		
Tension (N)	0.85	2.3
C0 (m/s)	147.82 ± 0.0614	241.96 ± 0.0159
EI_W (Nm^2)	$2.13*10^{-7} \pm 1.3*10^{-8}$	$2.38*10^{-7} \pm 1.22*10^{-9}$

Dispersion Corrected Dipole

Using the wave speed in the wire determined by equation 26, dispersive effects can be removed from the wave signal. This was done using another Matlab script. The dispersive wire displacement for the short pulse is described as $u_s(t) = \int_{-\infty}^{\infty} H(\kappa) e^{-i\omega t} d\omega$ where $H(\kappa) = \frac{I}{2\mu} \frac{e^{i\kappa c(\kappa)\delta t} - 1}{(\kappa c(\kappa))^2 (c + \kappa \frac{dc}{d\kappa})} \bar{B}(k)$. The dispersive solution is related to the non-dispersive solution by the scaling factor $F(\kappa)$; equation 23. The short or long pulse scaling factor is inserted into equation 24 to obtain a non-dispersive solution depending on which pulse wave is being analyzed. The process is described in more detail in Appendix A. The original wire displacement and dispersion corrected wire displacement from a short pulse, aka the first integral of the reference magnet, can be seen in Figure 31. The correccted signal has only small

distortions in the signal due to the low frequency noise in the measurements, and so provides a good representation of the non-dispersive solution.

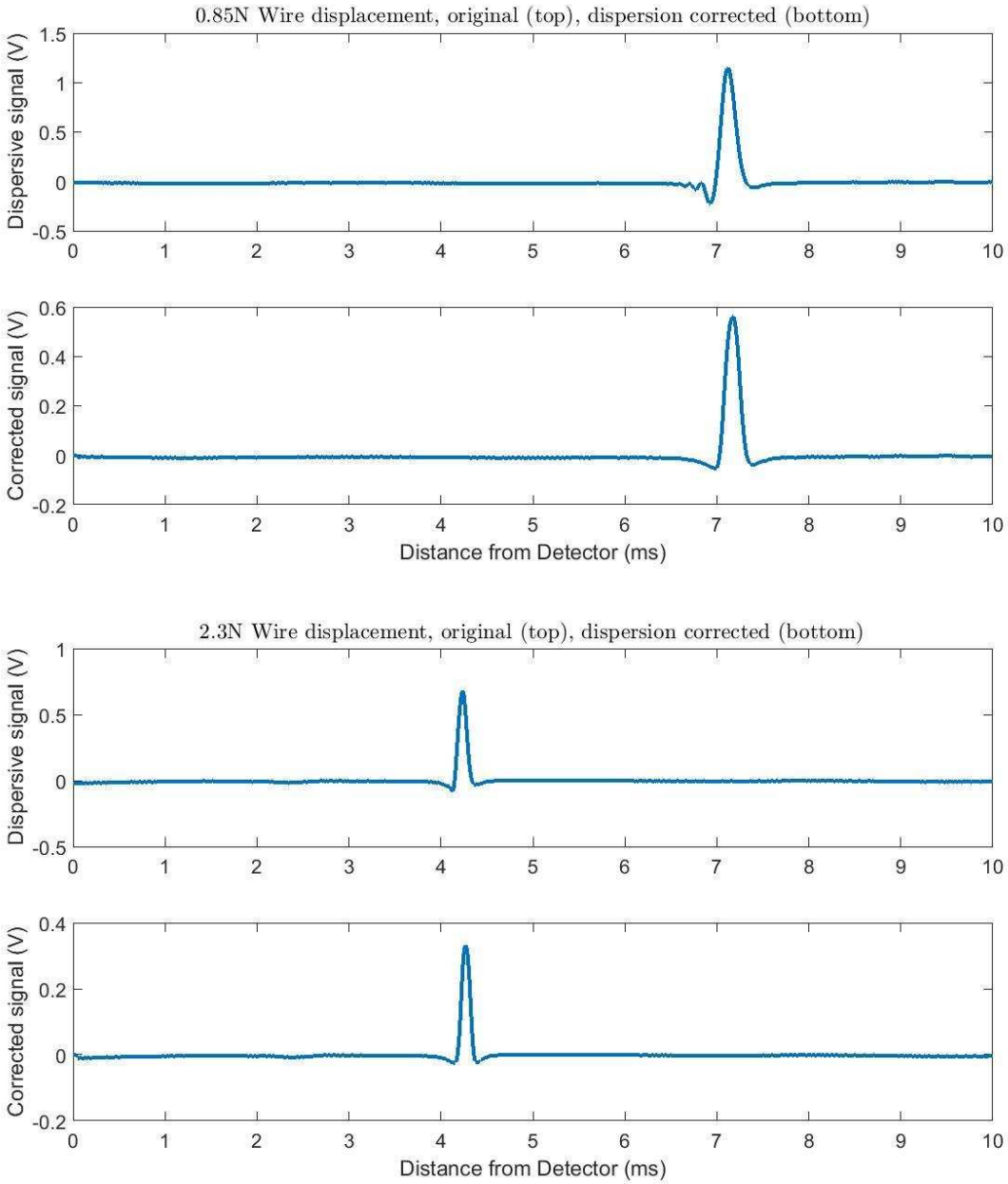

Figure 31: Uncorrected vs. corrected signal of the reference magnet for a short, $20\mu s$ pulse.

Distinguishable in both tension categories in Figure 31, is the removal of the dispersive components from the measured signal. However, the low tension measurement has much more dispersive effects and the correction is much more noticeable. Once corrected, the signals have a single specific wave speed over all frequency components; c_0.

The algorithm should function adequately for any tension. To verify this, a comparison of two different weighted signals was performed. Both signals were corrected for dispersion individually and then placed on a single plot (Figure 32). The corrected signals needed to be scaled such that the axis would line up correctly. The lower weight signal had greater amplitude and a stretched time axis due to a slower wave speed.

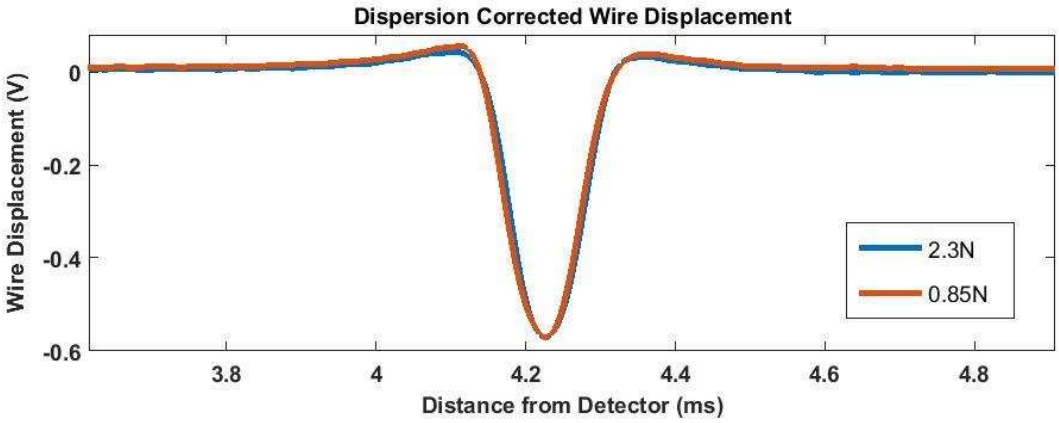

Figure 32: Dispersion corrected 1st field integral of 2.3N and 0.85N wire tension (scaled).

Comparing the corrected measurements from the low and high tension in Figure 32 one can see that the signals align nicely. This verifies the correctness of the algorithm for both tension schemes. For all final pulsed-wire measurements, the lower tension will be used.

The dispersive and non-dispersive wire displacements due to a long pulse (the second field integral) across the reference magnet are shown in Figure 33. The Matlab script created for dispersion correction in this case utilizes the scaling factor for a long pulse; Equation 25.

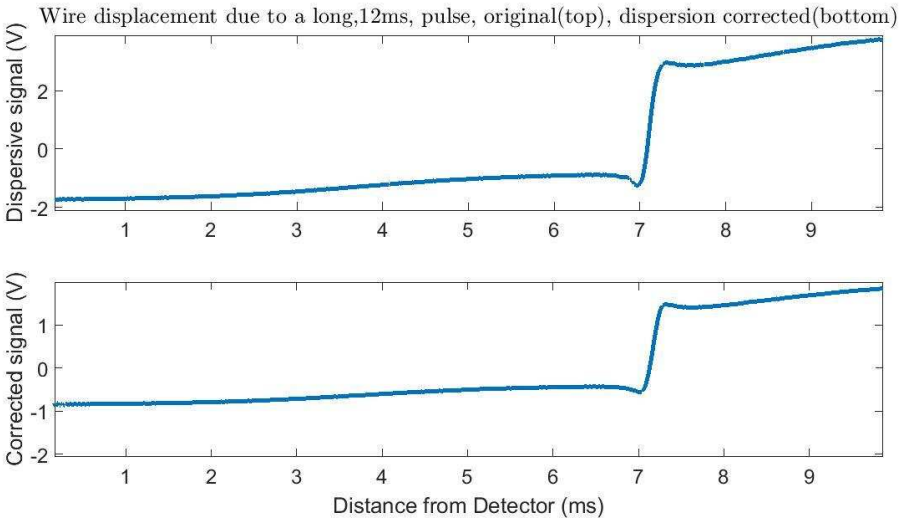

Figure 33: Uncorrected vs. corrected signal of the reference magnet for a long, 12ms, pulse.

In order to show that the algorithm works for both the long and short pulses. The corrected wire displacement due to the short pulse is compared to the first derivative of the corrected wire displacement due to the long pulse in Figure 34.

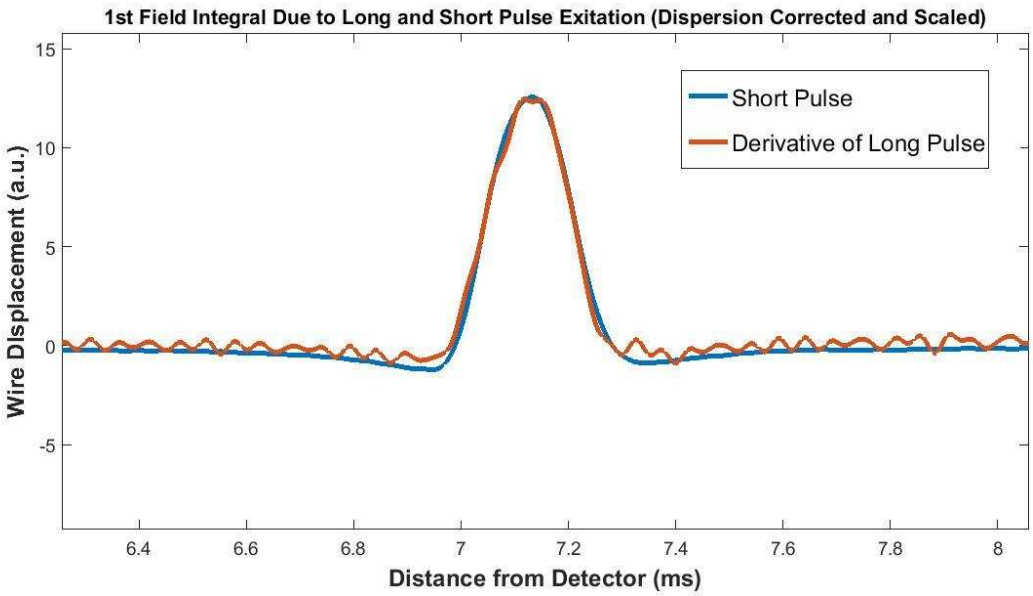

Figure 34: Corrected 1st field integral; short pulse compared to derivative of long pulse (scaled for comparison).

From Figure 34, the signal shapes agree nicely although the derivative signal is very noisy. This proves the effectiveness of the algorithms to remove dispersion from the signal and can now be used with high confidence for final measurements.

PW vs. Hall probe

The associated local magnetic field can be found by taking either the first or second derivative of the dispersion corrected signal, u_{s0}, depending on whether a short or long current pulse was applied. Once the B-field is found from this corrected displacement it needs be compared to the Hall probe data for accuracy and absolute scaling. Figure 35 shows the corrected pulsed-wire data as it compares to the Hall probe measurements.

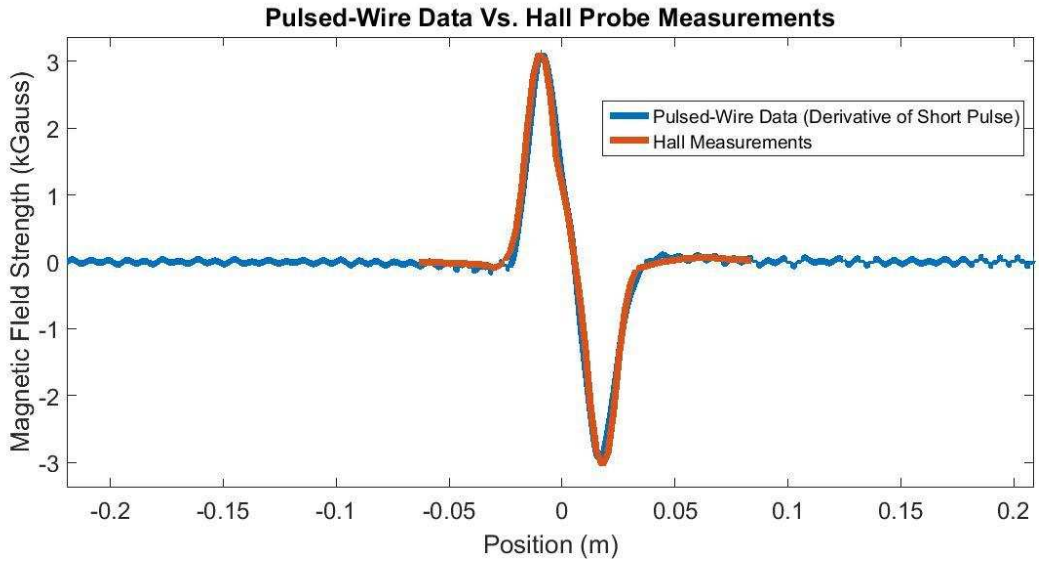

Figure 35: Comparison of the Hall probe and dispersion corrected pulsed wire measurements.

Note, the derivative of the short pulse measurement is compared to the Hall probe data in Figure 35. The experimental absolute scaling factor for the magnetic field was found to be $5 * 10^{-4}$, compared to the value calculated from Equation 24; $\frac{\mathrm{Ic_0\delta t}}{2\mathrm{T}} = 6.5 * 10^{-4}$. Again, the noise from the derivative calculation is visible but low enough such that the wave clearly keeps the true field profile. The comparison of the two data sets show that the pulsed-wire method can be used as an accurate representation of the local magnetic field with the correct scaling factor applied.

Dispersive and Corrected Pulsed-Wire Measurements of the Undulator

The uncorrected measured field of the undulator with a short pulse is shown in Figure 36 as well as the signal with the correction algorithm applied. This is the raw data collected from the oscilloscope due to a 20 μs current pulse.

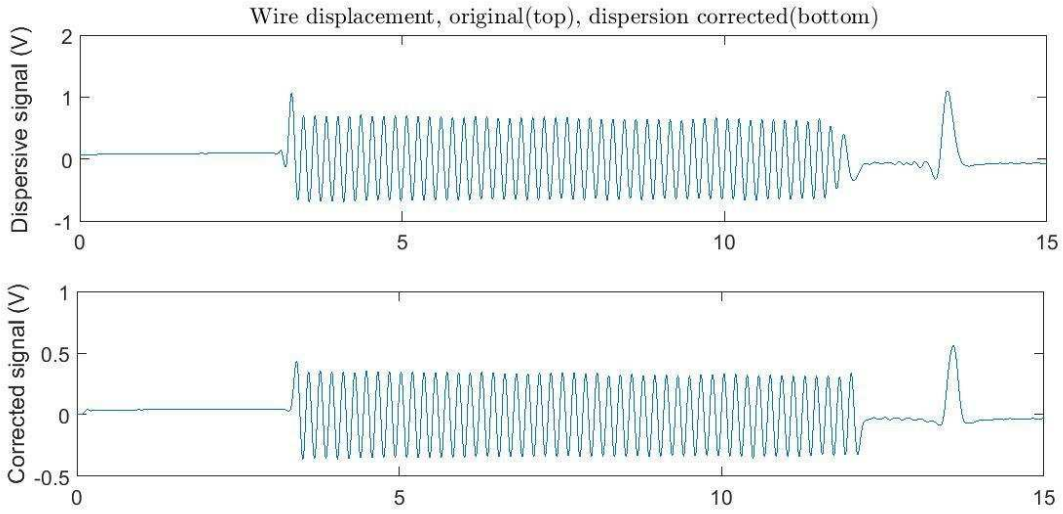

Figure 36: Uncorrected undulator and reference magnet measured signal due to the short pulse.

Here one can clearly see the dispersive effects in the measured signal, specifically at the tail end of the undulator. With the correction algortithm applied, the dispersion is removed. However, a small noise component is visible between the tail end of the undulator and the reference dipole. This, we believe, is an artifact due potentially to a small kink in the wire located midway into the undulator magnet.

The measured field from a long pulse is shown in Figure 37. Again, the raw data obtained from a 12ms current pulse is shown along with the dispersion corrected signal.

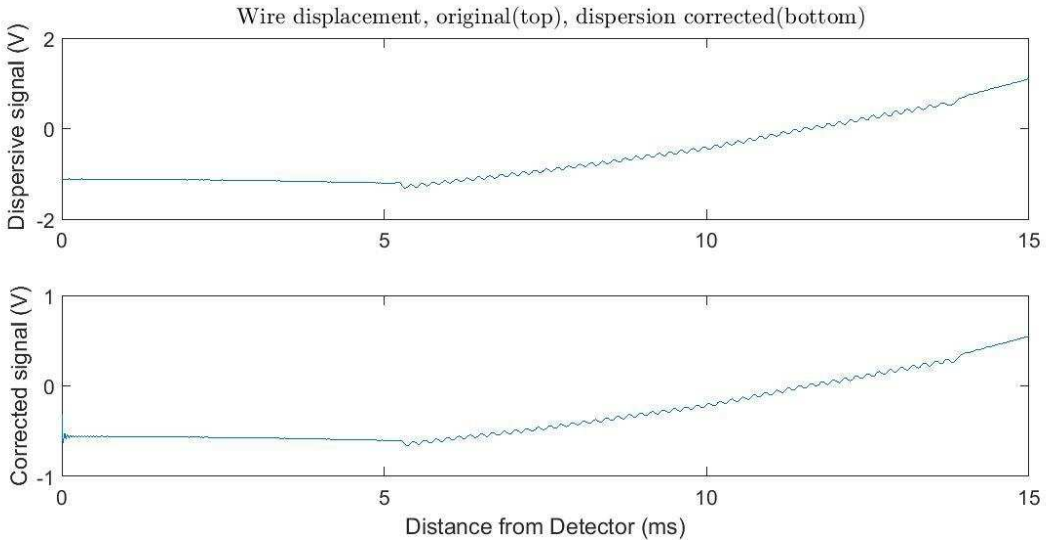

Figure 37: The measured signal from the long pulse.

As can be seen in Figure 37, there are no major deviations in the overall slope of the signal; however, there is a significant kick at the entrance to the undulator indicating that there is a mistuning present at that location. It is hard to see the correction of the dispersion as the slope dominates the scale.

Magnetic Field: Undulator

The final step in this thesis was to find the local absolute magnetic field of the CSU undulator magnet. The derivative of the dispersion corrected signal from Figure 36 was taken and then multiplied by the final scaling factor to gain the final magnetic field profile. This field is plotted in Figure 38.

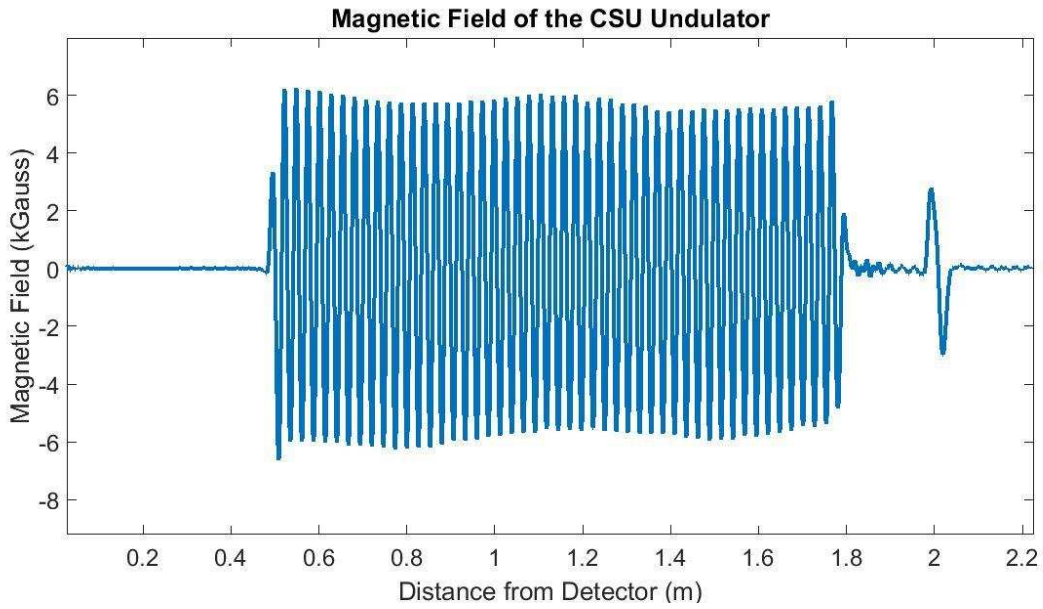

Figure 38: Local magnetic field of the undulator and reference magnet.

The final local magnetic field profile of the undulator is shown in Figure 38. Again, noise can be seen in the signal, but the exact shape of the profile can be easily determined. Thoughts on how to make more accurate and minimize noise even further are presented in a later section. This data will be used later for determining errors as well as in the verification of field corrections.

Next Steps

Determining the Errors and Shimming

The non-dispersive first and second field integrals have been determined. Now the trajectory and phase errors can be found using this data. These errors need to be within specific constraints, not covered here, for the FEL to function efficiently. To reduce errors that are outside these bounds, problem poles must be corrected.

The undulator device that is being measuring is “powered” by permanent magnets. Thus, we can merely shunt field away from locations and direct it elsewhere. This is done using ferromagnetic shims (Figure 39-left). By utilizing different shim placement techniques, one can solve angular, phase, and offset errors. The corrected fields can then be verified using the pulsed wire method.

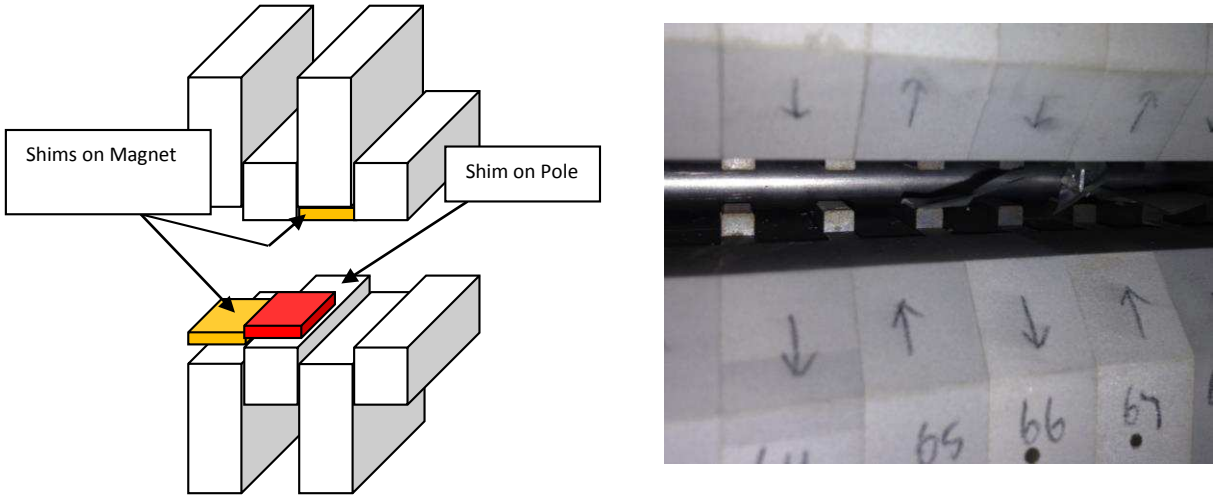

Figure 39: Shims can be placed on magnet or pole faces for desired effect (left). Dislodged shim on the CSU undulator (right).

By inspection (Figure 39-right), it can be seen that a previously placed shim has been dislodged from its original orientation during transport. Thus, at least one location on the undulator needs correction before operation [27].

System Difficulties

Noise Issues

Noise within the pulsed wire measurement has been a major hurdle for this project. Due to the sensitivity of the detector, environmental noise easily shows up on the measurements. The first noticeable area that affected the data was air flow within the lab. This air flow

perturbed the wire significantly and readily showed up as an erroneous random displacement. To overcome this, a 1” copper pipe was inserted around the wire to shield it as much as possible from air currents.

Due to equipment constraints, the setup was mounted across two separate optical tables. Differential movement between the tables during measurements was a valid concern. Therefore, a thick 1” aluminum plate was created to lock the two tables together to prevent any separate movement of the tables. The plate was designed in SolidWorks and used 50 optical screws to lock the two tables together. Connecting the plate was a delicate process because of the amount of force that can be exerted by the tables.

Another area that contracted a significant amount of noise was due to poor isolation of the optical tables from the ground. The room in which the system was housed was right next to the CSU engineering research center hydrology laboratory where they regularly flow thousands of gallons of water a minute for measurement of a multitude of hydrologically interesting things. The net result is significant ground vibrations and these vibrations were readily observable in the data. Many techniques to more efficiently isolate the tables were attempted, such as lifting the table off the isolating pneumatic cylinders using a jack and repositioning the legs to be more centered. Moving the undulator to displace the weight across the two separate tables equally was also tried. However, this made matters worse as it moved the center of gravity away from the center of the larger table and made the system more prone to sensing the ground vibrations. Ultimately, adjusting the tables’ legs and increasing the air pressure of the table isolation mounts proved to best dampen vibrations.

Even with all these adjustments, low-frequency noise components are significant in the measurements. Specifically, a large 60 Hz signal is contained within the wave as seen in Figure 40. Possible causes of these low-frequency components are electrical noise from cabling or other equipment, the pulse shape from the pulsing circuit not being adequate, or possibly still poor table isolation. Averaging on the oscilloscope can be used to reduce these noise effects, but they can still be seen in the wave speed calculation in an earlier section.

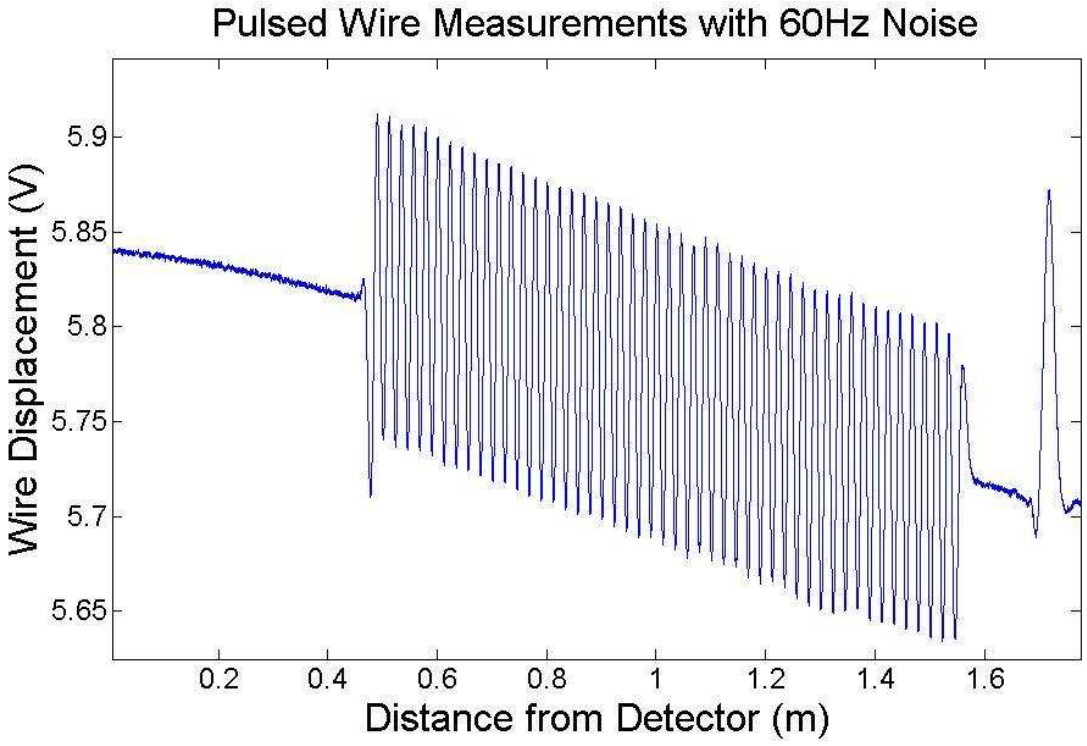

Figure 40: Noticeable noise in the pulsed wire measurements.

System Limitations

Along with the noise issues are limitations on the system due to available equipment. To get the resolution desired, 1 Gauss, the oscilloscope must have the capacity to take

measurements at the correct level. Thus, for a field of 0.61T, an oscilloscope must have at least a 12-bit resolution. The current TDS model being used is only capable of 10-bits.

Higher accuracy measurements can also be obtained by using different techniques not possible at this time. The use of two detectors, one upstream and one downstream of the undulator, can be used for more precise measurements. Here, one takes two measurements of the same wave at different locations and averages them.

Another area of improving noise issues is to place the entire system under vacuum, which would eliminate most of the air flow noise of the system. However, this would be extremely costly and not practical for our current experiments.

The final area of improvement is with the reference magnet characteristics. Having net zero first and second field integrals will make measurements easier. For a long pulse, the “step” in the signal would be removed. After the reference signal, the voltage level will be returned to the original position, ready for the undulator signal to be measured more accurately. Next, by having a reference magnet with top and bottom poles, the distance of the wire above the magnet never needs to be measured. This can be done by placing fiducialization marks on the reference magnet to quickly and accurately place the wire at any time. The final reference magnet improvement is making the poles skinnier. This will create higher frequency components in the wave speed calculation resulting in more accurate dispersion correction. These improvements can be utilized for higher accuracy and better overall measurements.

Conclusions

A pulsed-wire method has been developed and used to characterize the magnetic field of CSU's undulator magnet. A reference magnet was built and mapped thoroughly using a Hall probe. Measurements of the reference magnet were done with the pulsed-wire technique for comparison and absolute scaling. The mechanical and magnetic centers of the undulator have been found and final measurements were taken at the latter. Algorithms were developed in Matlab to determine the dispersive wave speed in the wire and also correct the data for dispersion and finite-pulse width errors. These algorithms were applied to both the reference magnet and undulator fields respectively as well as in conjunction with each other. For future work, the magnetic field errors need to be corrected using small magnetic shims. The results given are reproducible, within the noise error, and the method can be used for many different types of magnets in the future for ultra-fast field characterization.

REFERENCES

[1] “Basics of Synchrotron Radiation Beamlines and Detectors”, University of Chicago, USA, retrieved March 2015 from: http://cars9.uchicago.edu/xafs_school/APS_2005/Heald_Instrument.pdf

[2] “Beamlines”, Advanced Photon Source, Argoone, USA, retrieved February 2015 from: https://www1.aps.anl.gov/Beamlines

[3] Biedron, S. et al., “Accelerators for Americas Future”, U.S. Department of Energy, retrieved May 2014 from: http://science.energy.gov/~/media/hep/pdf/accelerator-rd-stewardship/Report.pdf

[4] Schmuser, P., “Free Electron Lasers,” University of Hamburg, retrieved May 2015 from: https://cas.web.cern.ch/cas/ZEUTHEN/Zeuthen-talks/250903/schmueser-fel.pdf

[5] Thompson N., “Introduction to Free-Electron Lasers,” ASTeC, 4GLS, retrieved Dec. 2014 from: http://www.astec.stfc.ac.uk/ASTeC/Resources/PDF/Thompson_FELs.pdf

[6] Neil, G.R., “FEL Transformation”, SPIE Professional, October 2009, retrieved March 2015 from: http://spie.org/x37534.xml

[7] Barletta, W. A., “Unit 11 - Lecture 18 Synchrotron Radiation-1,” U.S. Particle Accelerator School, University of New Mexico, 2009. Retrieved June 2015 from: http://uspas.fnal.gov/materials/09UNM/Unit_11_Lecture_18_Synchrotron_radiation.pdf

[8] Attwood, D., “Intro to Synchrotron Radiation: Bending Magnet Radiation,” Univ. California, Berkeley, EE290F, 8 Feb. 2007

[9] Chavanne, J., “The art of the undulator”, ESRF, January 2012, retrieved February 2015 from: http://www.esrf.eu/Accelerators/news/art-undulator

[10] McNeil, B. W. J. & Thompson, N. R., “X-ray free-electron lasers,” Nature Photonics 4, 814–821 (2010)

[11] Workie, D. W., “Basic Physical Processes and Principles of Free Electron Lasers (FELs)”, Department of Physics, University of Cincinnati, Cincinnati, Ohio, USA, 2001

[12] Attwood, D., “Undulator Equation and Radiated Power”, EE290F, 15 Feb 2007, University of California, Berkeley, http://www.coe.berkeley.edu/AST/srms

[13] Gehlot, M., Mishra, G., “An overview of the undulator field measurement studies at insertion device lab, DAVV” J. Phys.: Conf. Ser. 365 (2012) 012052

[14] Bahrdt, J., “Operation of APPLE Undulators @ BESSY II”, 48th ICFA Advanced Beam Dynamics Workshop on Future Light Sources March 1-5, 2010, SLAC National Accelerator Laboratory, Menlo Park, Ca, USA

[15] Verschuur, J.W.J., Warren, R.W., “Tuning and characterization of Twente wiggler”, Nucl. Instr. & Meth. A 375 (1996) 508-510

[16] Chavanne, M., Hahn, R., Kersevan, C.A., Kitegi, C. Penel, F. Revol, ESRF, Proceedings of EPAC 08, WEPC105, Genoa, Italy, 2008, p. 2243

[17] S. Popovich, 9th International Magnetic measurement workshop, CEA/Saclay, June, 1995

[18] Vall´eau, M., Benabderahmane, C., “ Measurements of soleil insertion devices using pulsed wire method”, Proceedings of IPAC2011, San Sebastián, Spain, 2011

[19] Ernst, G.J. et. al., “The ‘TEUFEL’ project”, W.J., Nucl. Instr. & Meth. A 318 (1992) 847-852

[20] Arbelaez, D., Wilks T. et al., “A dispersion and pulse width correction algorithm for the pulsed wire method”, Nucl. Instr. & Meth. in Phys. Res. A 716 (2013) 62-70

[21] R. W. Warren, “Limitations on the use of the pulsed– wire field measuring technique”, Nucl. Instr. and Meth., A272 (1988) 257

[23] O. Shahal and R. Rohatgi, “Pulsed Wire Magnetic Field Measurements on a 4.3m long wiggler”, Nucl. Instr. and Meth., A285 (1989) 299-302

[22] Fan, T. C., Lin, F.Y. et al., “Pulsed wire magnetic field measurements on undulator U10P”, Proceedings of PAC2001, Chicago, USA, 2001, p. 2775-2777

[24] Tripathi, S., Gehlot, M. et al., “Field integral measurement of a six period undulator in a pulsed wire set up”, Optics Communications 284 (2011) 350–357

[25] Travish, G., Rosenzweig, J., “Strong sextupole focusing in planar undulators”, Nucl. Instr. & Meth. A 345 (1994) 585-593

[26] Henderson, J. R., Campbell, L.T., “The implementation of 3D undulator fields in the unaveraged fel simulation code Puffin”, Proceedings of FEL2014, TUP022, Basel, Switzerland, 2014

[27] Yuhui Li and Joachim Pflueger, “Tuning method for phase shifters with very low first field integral errors for the European X-ray Free Electron Laser,” Phys. Rev. ST Accel. Beams 18, 030703, 6 March, 2015.

APPENDIX A: PULSED WIRE THEORY

The following section follows [20] closely and is the theory behind the "wave speed determination" and "dispersion correction" algorithms implemented in Matlab. The 5-step algorithm used to correct for dispersion and finite pulse widths in this thesis can be found at the bottom.

The velocity and position of an electron in an undulator are described by the first and second integrals of the magnetic field. Since the result of a pulse in the a magnetic field in a pulsed-wire system produces an acoustic wave, the displacement of the wire can be described by a general traveling wave equation:

$$u(z,t) = \int_{-\infty}^{\infty}\left[D_1(\kappa)e^{-i(\kappa z-\omega t)} + D_2(\kappa)e^{-i(\kappa z+\omega t)}\right]d\kappa \qquad \text{(A1)}$$

Here, $u(z,t)$ is the wire displacement at some location z and time t. κ is the wave number, ω is the frequency and are related to the wave speed by the relation $c = \frac{\omega}{\kappa}$. D_1 and D_2 are functions and are found by initial conditions. When dispersion is present in the wire, c is no longer a constant and becomes a function of the wave number, $\omega = c(\kappa)\kappa$. If a square pulse is sent through the wire at time t=0, the displacement of the wire due to a magnetic field is

$$u_s(t) = \frac{I}{2\mu}\int_{-\infty}^{+\infty}\frac{e^{i\omega\delta t}-1}{\omega^2}\bar{B}(\kappa)e^{-i\omega t}d\kappa$$

$$= \frac{I}{2\mu}\int_{-\infty}^{+\infty} -\frac{\bar{B}(\kappa)}{\omega^2}e^{-i\omega t}d\kappa + \frac{I}{2\mu}\int_{-\infty}^{+\infty}\frac{\bar{B}(\kappa)}{\omega^2}e^{-i\omega(t-\delta t)}d\kappa = u_{s1}(t) + u_{s2}(t) \qquad \text{(A2)}$$

Here, $u_s(t)$ is the displacement of the wire in the time domain, μ is the density of the wire, I is the amplitude of the current pulse,and $\bar{B}(\kappa) = \mathcal{F}[B(x)]$ is the Fourier transform of the magnetic field, B. Here, we assume that the magnetic field is positioned at some location z>0 and the sensor lies at z=0.

For the non-dispersive case, the wave frequency is $\omega = c_0\kappa$, where $c_0 = \sqrt{\frac{T}{\mu}}$. T is the tension of the wire. Assuming the displacement and velocity of the wire are zero at the sensor, Equation A2 becomes:

$$u_{s0}(t) = \frac{I}{2T}\int_{c_0(t-\delta t)}^{c_0 t}\int_0^{\bar{z}} B(\hat{z})d\hat{z}d\bar{z} \tag{A3}$$

The subscript 0 indicates the non-dispersive case. As $\delta t \to 0$ and keeping $I\delta t$ constant, (A3) becomes:

$$u_{s0}(t) = \frac{Ic_0\delta t}{2T}\int_0^{c_0} B(\bar{z})d\bar{z} \tag{A4}$$

Equation A4 shows that the motion of the wire is proportional to the first integral of the magnetic field and thus, the velocity of a charged particle traveling through the wire. This is used for the representation of a “short” current pulse in the wire. To find the effect of a “long” pulse, $c_0\delta t$ must be larger than the magnetic field of the undulator, or $\delta t > N\lambda_u$. So, (A3) reduces to:

$$u_{s0}(t) = \frac{I}{2T}\int_0^{c_0 t}\int_0^{\bar{z}} B(\hat{z})d\hat{z}d\bar{z} \tag{A5}$$

This equation describes the position (trajectory) of a charged particle traveling along the wire is proportional to the second integral of the magnetic field of the undulator. So, a "long" current pulse will give information about the second field integral and the position of the particle.

It was assumed previously that $\delta t \to 0$, but in reality δt will have some finite width. Dispersion, due to the finite flexural rigidity of the wire, was also assumed to be nonexistent. To accurately determine the movement of the wire due to the magnetic field, these need to be incorporated into the equation of motion. For dispersion correction, the wave speed in the wire must be determined and related to the frequency. First, Equation (A2) is transformed from the κ-domain to the ω-domain:

$$u_s(t) = \frac{I}{2\mu}\int_{-\infty}^{+\infty} \frac{e^{i\omega\delta t}-1}{\omega^2(c+\kappa\frac{dc}{d\kappa})}\bar{B}(\kappa)e^{-i\omega t}d\omega = \int_{-\infty}^{+\infty} G(\omega)e^{-i\omega t}d\omega. \qquad \text{(A6)}$$

and

$$G(\omega) = \frac{I}{2\mu}\frac{e^{i\omega\delta t}-1}{\omega^2(c+\kappa\frac{dc}{d\kappa})}\bar{B}(\kappa).$$

$G(\omega)$ is introduced for simplicity and can be found by taking the Fourier transform of $u_s(t)$.

To calculate the wave speed, two experimental measurements of a reference magnet must be made. Where the second measurement is taken with the magnetic field, or detector, displaced a distance Δz from the location of the first. The wire displacement with the displaced magnet is:

$$u_{s\Delta z}(t) = \frac{I}{2\mu}\int_{-\infty}^{+\infty} \frac{e^{i\omega\delta t}-1}{\omega^2}\bar{B}(\kappa)e^{i\kappa\Delta z}e^{-i\omega t}d\kappa$$

$$= \int_{-\infty}^{+\infty} G(\omega) e^{i\kappa\Delta z} e^{-i\omega t} d\omega \quad \text{(A7)}$$

Where $\bar{u}_{s\Delta z} = G(\omega)e^{i\kappa\Delta z}$ is found by taking the Fourier transform of $u_{s\Delta z}(t)$ into. Multiplying the conjugate of $\bar{u}_s(\omega)$ by $\bar{u}_{s\Delta z}(\omega)$ gives

$$\bar{u}_s^*(\omega)\bar{u}_{s\Delta z}(\omega) = |G(\omega)|^2 e^{i\kappa\Delta z} \quad \text{(A8)}$$

This says that the product has an amplitude, $|G(\omega)|^2$, and phase $\phi = \kappa\Delta z$. By using the relation that $\omega = c\kappa$, the wave speed can be found:

$$c = \frac{\omega\Delta z}{\phi} \quad \text{(A9)}$$

This equation shows the wave speed as a function of frequency for experimental results by moving the detector or reference magnet by Δz.

Using the Euler-Bernoulli theory for the bending of thin rods, a theoretical value of the wave speed can be found. The transverse wave motion, u, for a Euler-Bernoulli beam (tensioned) is described as:

$$T\frac{\partial^2 u}{\partial z^2} - EI_w\frac{\partial^4 u}{\partial z^4} = \mu\frac{\partial^2 u}{\partial t^2} \quad \text{(A10)}$$

where E is the Young's modulus of the wire material (in this case BeCu) and I_w is the moment of inertia of the wire. The traveling wave solution, $e^{-i\kappa(z-ct)}$, can be added to Equation A10 and the Euler-Bernoulli dispersion relation can be found:

$$c(\kappa) = c_0\sqrt{1 + \frac{EI_w}{T}\kappa^2} \quad \text{(A11)}$$

This equation is used as a fit for the experimental data, because it is a general dispersion equation. However, the EI_w parameter has high uncertainty and may need updating for correct fitting.

Now that the dispersion characteristics have been determined, a correction algorithm can be implemented to improve the accuracy of the method. The algorithm will be different for both the "short" and "long" pulse lengths. The algorithm for the "short" pulse also corrects errors due to the finite pulse width. Equation A2 can be rewritten to become

$$u_s(t) = \frac{I}{2\mu}\int_{-\infty}^{+\infty} \frac{e^{i\kappa c\delta t}-1}{\left(\kappa c(\kappa)\right)^2\left(c+\kappa\frac{dc}{d\kappa}\right)} \bar{B}(\kappa)e^{-i\omega t}d\omega = \int_{-\infty}^{+\infty} H(\kappa)e^{-i\omega t}d\omega \qquad \text{(A12)}$$

Where:

$$H(\kappa) = G\big(\omega(\kappa)\big) = \frac{I}{1\mu}\frac{e_0^{i\kappa c\delta t}-1}{\left(\kappa c(\kappa)\right)^2(c+\kappa\frac{dc}{d\kappa})}$$

For the non-dispersive case, Equation A12 is:

$$u_{s0}(t) = \frac{I}{2\mu}\int_{-\infty}^{+\infty} \frac{e^{i\kappa c_0\delta t}-1}{\kappa^2 c_0^3} \bar{B}(\kappa)e^{-i\omega t}d\omega = \int_{-\infty}^{+\infty} H_0(\kappa)e^{-i\omega t}d\omega$$

$$= \int_{-\infty}^{+\infty} F(\kappa)H(\kappa)e^{-i\omega t}d\omega \qquad \text{(A13)}$$

From equations A12 and A13, $F(\kappa) = \frac{H_0(\kappa)}{H(\kappa)}$ where $H_0 = \frac{I}{2\mu}\frac{\left(e^{i\kappa c_0\delta t}-1\right)}{\kappa^2 c_0^3}$. $F(\kappa)$ is a scaling function that correlates the dispersive ($u_s(t)$) and non-dispersive ($u_{s0}(t)$) solutions. To determine the non-dispersive solution, the Fourier transform of $u_s(t)$ is taken to find $H(\kappa)$. Then $H_0(\kappa)$ can then be found by multiplying $F(\kappa)$ and $H(\kappa)$. The non-dispersive solution, u_{s0}, can then be

acquired by applying the inverse Fourier transform. The scaling function, F, will be determined for both short and long pulses.

In order to use equation A13, $u_s(t)$ first needs to be transformed into the κ domain. So a Fourier transform needs needs to be applied.

$$H(\kappa) = G\big(\omega(\kappa)\big) = \frac{1}{2\pi}\int_{-\infty}^{+\infty} u_s(\tau)e^{i\omega(\kappa)\tau}d\tau \tag{A14}$$

To implement this in software, a discrete transform is needed with evenly spaced values of ω, ω_i. Equation A14 becomes

$$H\big(\kappa(\omega_i)\big) = G(\omega_i) = \frac{1}{2\pi}\int_{-\infty}^{+\infty} u_s(\tau)e^{i\omega_i\tau}d\tau \tag{A15}$$

Using the appropriate scaling function, a discrete form of equation A13 can be used to determine the non-dispersive displacement.

$$u_{s0}(t_i) = c_0\int_{-}^{+} H_0(\kappa)e_0^{-ic_0\kappa t_i}d\kappa \tag{A16}$$

For a short current pulse, taking the limit as $\delta t \to 0$ to account for finite pulse width errors, Equation A13 becomes:

$$u_{s0}^{short}(t) = \frac{I\delta t}{2\mu}\int_{-\infty}^{+\infty}\frac{i}{\kappa c_0^2}\bar{B}(\kappa)e^{-i\omega t}d\omega \tag{A17}$$

Where $\bar{B}(\kappa)$ is related to $H_0(\kappa)$ by:

$$H_0^{short}(\kappa) = \frac{I\delta t}{2\mu}\frac{i}{\kappa c_0^2}\bar{B}(\kappa) \tag{A18}$$

Comparing Equation A12 and A18, the scaling factor for the short pulse is:

$$F^{short}(\kappa) = \frac{H_0(\kappa)}{H(\kappa)} = \left(\frac{c(\kappa)}{c_0}\right)\left(\frac{c(\kappa)+\kappa\frac{dc}{d\kappa}}{c_0}\right)\frac{i\omega(\kappa)\delta t}{e^{i\omega(\kappa)\delta t}-1} \quad \text{(A19)}$$

The length (δt) of the short pulse must be chosen such that $\omega_{max}\delta t < 2\pi$ to prevent singularities. ω_{max} is the maximum frequency of the pulsed wire signal.

For the case of a long pulse, where $c_0\delta t$ is greater than the total length of the undulator, Equation A12 can be rewritten as:

$$u_s^{long}(t) = -\frac{I}{2\mu}\int_{-\infty}^{+\infty}\frac{1}{(\kappa c(\kappa))^2\left(c+\kappa\frac{dc}{d\kappa}\right)}\bar{B}(\kappa)e^{-i\omega t}d\omega = \int_{-\infty}^{+\infty}H(\kappa)e^{-i\omega t}d\omega \quad \text{(A20)}$$

By comparison, Equation A13 (non-dispersive) becomes:

$$u_{s0}^{long}(t) = -\frac{I}{2\mu}\int_{-\infty}^{+\infty}\frac{1}{\kappa^2 c_0^3}\bar{B}(\kappa)e^{-i\omega t}d\omega = \int_{-\infty}^{+\infty}H_0(\kappa)e^{-i\omega t}d\omega \quad \text{(A21)}$$

In order to get $H_0(\kappa)$ from $H(\kappa)$ from the previous two equations, the scaling factor can be found to be:

$$F^{long}(\kappa) = \frac{H_0(\kappa)}{H(\kappa)} = \left(\frac{c(\kappa)}{c_0}\right)^2\frac{c(\kappa)+\kappa\frac{dc}{d\kappa}}{c_0} \quad \text{(A22)}$$

The scaling factor for both the long and short pulses will make it possible to get a non-dispersive solution from the dispersive solution.

Correction algorithm Summary [20]:

"1. Set evenly spaced ω_i over a large enough range to correctly capture $B(\kappa(\omega))$.

2. For all ω_i numerically integrate Equation A15 to obtain $G(\omega_i)$.

3. Calculate unevenly spaced κ values, $\kappa_i = \kappa(\omega_i)$, which are associated with $H(\kappa_i) = G(\omega_i)$.

4. Multiply $H(\kappa_i)$ by $F(\kappa_i)$ to obtain $H_0(\kappa_i)$ (use Equation A19 for short pulse and A22 for long pulse).

5. For each time t_i numerically integrate Equation A16 to determine the non-dispersive displacement solution $u_{s0}(t_i)$."